



# Corrosion and passivation behavior of laser powder bed fusion produced Ti-6Al-4V in static/dynamic NaCl solutions with different concentrations

P. Qin<sup>a</sup>, L.Y. Chen<sup>b,\*</sup>, Y.J. Liu<sup>a</sup>, Z. Jia<sup>a</sup>, S.X. Liang<sup>a</sup>, C.H. Zhao<sup>c</sup>, H. Sun<sup>a</sup>, L.C. Zhang<sup>a,\*</sup>

<sup>a</sup> School of Engineering, Edith Cowan University, 270 Joondalup Drive, Joondalup, Perth, Western Australia, 6027, Australia

<sup>b</sup> School of Material Science and Technology, Jiangsu University of Science and Technology, Zhenjiang, Jiangsu, 212003, China

<sup>c</sup> Guangxi Key Laboratory of Processing for Non-ferrous Metals and Featured Materials, Guangxi University, Nanning, 530004, China

## ARTICLE INFO

### Keywords:

Laser powder bed fusion  
Titanium  
Corrosion  
Oxide film  
NaCl  
Dynamic solution

## ABSTRACT

In this work, the corrosion and passivation behavior of Ti-6Al-4V produced by laser powder bed fusion (L-PBF) were investigated in different concentration of NaCl solutions under static and dynamic conditions. Oxide films including TiO<sub>2</sub>, Ti<sub>2</sub>O<sub>3</sub>, TiO were formed on L-PBF-produced Ti-6Al-4V. The film thickness increased under both test conditions with increasing the Cl<sup>-</sup> concentration, and the film contained more TiO<sub>2</sub> in dynamic conditions under the same Cl<sup>-</sup> concentration. The mechanism of the corrosion behavior and film growth under different Cl<sup>-</sup> concentration and electrolyte conditions were discussed by the relevant electrochemical and surface characteristic measurements, e.g. Mott-Schottky analysis, X-ray photoelectron spectroscopy.

## 1. Introduction

Over the past few decades, additive manufacturing (AM) technologies have attracted considerable attention in fabricating metallic components because of their advantages in complex-shape design, no requirement of additional post-processing, compatibility with multiple metal types, high material utilization rate, and short production cycle, etc. [1,2]. AM is widely employed in manufacturing components for chemical plants, aerospace applications, marine industries, biomedical purposes, etc. [3–5]. Selective laser melting (SLM), also known as laser powder bed fusion (L-PBF), is one of the most commonly used powder bed fusion technologies in AM technologies to manufacture metallic materials [6,7]. L-PBF uses a high-energy laser as the input heat source to melt the selected areas on a pre-deposited layer of metal powder. The powdering and laser melting processes are then repeated until the entire production is finished [8]. At present, a variety of metallic materials including titanium (Ti) alloys [9–11], aluminum (Al) alloys [12–15], stainless steels [16–18], Co-Cr-based alloys [19–21] and metallic glasses [22–24], etc. have been successfully prepared by SLM. These SLM-produced (SLMed) components usually exhibit comparable or even enhanced mechanical properties and corrosion resistance compared to their conventional counterparts because of their refined microstructures resulted from the rapid solidification ( $10^5 \sim 10^8$  K/s) of the molten pool during the manufacturing process [25,26].

The corrosion behavior of L-PBF-produced alloys has received increasing attraction in recent years. It is well accepted that the metallic materials would irreversibly undergo severe corrosion in the period of their services, which becomes a severe problem. Fortunately, most alloys manufactured by L-PBF display a comparable and even enhanced corrosion resistance compared to those of the conventional counterparts [27,28]. For example, the SLMed AlSi10Mg alloy (with Si content of 9–11 wt%) and SLMed Al-12Si (with Si content of 12 wt%) present an enhanced pitting corrosion resistance compared with their conventional counterparts, which is attributed to the refined cellular microstructure formed during the SLM process. Such a cellular microstructure is mainly composed of supersaturated Al-rich primary phase and refined Si particles locating at the grain boundaries of the primary phase [29]. The SLM process could also improve the pitting resistance of a 316 L stainless steel (SS) by eliminating manganese sulfide (MnS) inclusions, which are prone to trigger their pitting corrosion caused by the conventional manufacturing process [30]. Furthermore, the SLMed Ti-6Al-4V usually displays a microstructure with a dominant acicular  $\alpha'$  phase that is extremely different from those in the conventionally manufactured counterparts, resulting in a comparable corrosion behavior [31]. For example, Dai et al. [32] reported that the passivation current density of the SLMed Ti-6Al-4V is about twice that of the cast Ti-6Al-4V in 3.5 wt% NaCl solution, indicating that the oxide film formed on the cast Ti-6Al-4V is more compact than that formed on the SLMed Ti-6Al-4V.

\* Corresponding authors.

E-mail addresses: [lychen@just.edu.cn](mailto:lychen@just.edu.cn) (L.Y. Chen), [l.zhang@ecu.edu.au](mailto:l.zhang@ecu.edu.au), [lc Zhang@gmail.com](mailto:lc Zhang@gmail.com) (L.C. Zhang).

<https://doi.org/10.1016/j.corsci.2021.109728>

Received 31 May 2021; Received in revised form 18 July 2021; Accepted 26 July 2021

Available online 28 July 2021

0010-938X/© 2021 Elsevier Ltd. All rights reserved.

Hamza et al. [4] demonstrated that the SLMed Ti-6Al-4V has a lower corrosion current density compared to the wrought Ti-6Al-4V in artificial saliva, confirming the better corrosion resistance of SLMed Ti-6Al-4V. Zhang et al. [33] investigated the corrosion behavior of SLMed Ti-6Al-4V and wrought Ti-6Al-4V in artificial saliva with different fluoride concentrations and pH values, and their results indicated the wrought Ti-6Al-4V has significantly better corrosion resistance than the SLMed counterparts. Note that, the corrosion results reported in the above literature are based on the investigations in static electrolyte environments. However, most materials are substantially applied in dynamic electrolyte environments, such as marine, chemical industry, human body, and so on [33–36]. The corrosion behavior of SLMed alloys in the dynamic fluid has been rarely investigated [37] and thus is less understood.

On the other hand, the service environment is also one of the critical parameters that affect the corrosion resistance of the L-PBF-produced alloys. Toptan et al. [38] investigated the corrosion behavior of SLMed Ti-6Al-4V and commercial counterparts in 0.9 wt% NaCl solution and their results indicated that the SLM process led to a low-quality oxide film formed on SLMed Ti-6Al-4V. Yang et al. [39] investigated the corrosion behavior of Ti-6Al-4V manufactured by different manufacturing methods in 3.5 wt% NaCl solution. Their results indicated that SLMed Ti-6Al-4V showed the worst corrosion resistance, but the corrosion resistance was further improved by heat treatment at 300 °C. Li et al. [40] investigated the corrosion behavior of laser solid formed Ti-6Al-4V in a highly concentrated NaCl solution (15 wt%). The results showed that the corrosion resistance of the produced sample decreases with increasing the grain sizes. Most of the literature focused on the corrosion behavior of SLMed Ti-6Al-4V in the NaCl solution with a single concentration rather than in those with varying concentrations. Since the halide ion is harmful to the formed oxide film, the corrosion behavior of the sample would be altered as the NaCl concentration varies [41]. Furthermore, Renner et al. [42] summarized the excellent corrosion resistance of Ti alloys according to the formed oxide film on the sample surface when exposed to an oxygen-rich environment. However, the formation of the TiO<sub>2</sub> on Ti alloy in neutral solutions is dehydrated from the initial formed TiO and Ti<sub>2</sub>O<sub>3</sub> (suboxides), so that the oxide film formed on the Ti alloy surface could include TiO, Ti<sub>2</sub>O<sub>3</sub>, and TiO<sub>2</sub> [43–46]. Therefore, the thickness and characteristics of the oxide film are different when altering the testing solution, and further investigations on the corrosion mechanism and the oxide properties of the SLMed Ti-6Al-4V under different NaCl concentrations are needed.

It is well known that the corrosion resistance and mechanism of metals are mainly attributed to the properties of the oxide film formed on their surfaces, and the characteristics of the formed oxide film can be affected by several factors discussed above. Hence, this work aims to investigate the effect of environmental factors on the corrosion resistance and corrosion mechanism of the SLMed Ti-6Al-4V. The testing environments included 0.9, 3.5, and 10 wt% NaCl solutions, and the testing conditions of the solutions were set to static or dynamic conditions separately. Some electrochemical methods and characterizations were used to investigate the corrosion behavior and mechanism in different conditions. This work demonstrated that the higher concentration of Cl<sup>-</sup> promotes the growth kinetics of the film thereby forming a thick film with better corrosion resistance, but the film formed under dynamic conditions contains more defects with less thickness.

## 2. Experimental

### 2.1. Material preparation

A series of Ti-6Al-4V alloy samples with the dimensions of 7 mm × 7 mm × 7 mm were manufactured using a ReaLizer SLM 100 machine. The relative density, measured by Archimedes method, of the SLMed Ti-6Al-4V was above 99.5 %, resulted from the use of the optimal SLM manufacturing parameters as follows: laser power of 200 W, laser

scanning speed of 1000 mm/s, spot size of 40 μm, layer thickness of 50 μm, and hatching space of 100 μm. Each SLM-produced sample was drilled a penetrating hole on the middle-top side of the finished plane (XZ-plane), connected with a copper wire, and sealed in an epoxy resin. The sealed samples were ground with waterproof SiC papers up to 2000 grits and polished to a mirror finish with the standard fumed silica suspension (Struers, OP-S, 0.25 μm). The polished samples were ultrasonically cleaned in ethanol for 3 min and dried in air. The edges of all samples were sealed with silicone glue prior to electrochemical testing in order to prevent crevice corrosion.

### 2.2. Electrochemical measurements

The electrochemical measurements in this work were carried out by a three-electrode system and connected to an electrochemical workstation (Solartron, EchemLab). In the three-electrode system, the SLMed Ti-6Al-4V sample was employed as a working electrode, a 25 mm × 25 mm platinum mesh was used as a counter electrode, and a saturated calomel electrode (SCE, 0.242 V relative to the standard hydrogen electrode) was employed as a reference electrode. Therefore, all potentials reported in this work were referred to SCE.

The electrolyte was prepared using NaCl solutions (Sigma, CAS Number: 7647-14-5) with concentrations of 0.9, 3.5, and 10 wt%, respectively. The dynamic condition (flowing state) of the solution was simulated by a 2 cm PTFE (poly tetra fluoroethylene) stir bar and magnetic stirrer (VELP, Scientifica) at a rotate speed of 400 rpm. Therefore, the abbreviations S-0.9, S-3.5, S-10, D-0.9, D-3.5, and D-10 were used to describe the SLMed Ti-6Al-4V tested in 0.9, 3.5, and 10 wt % NaCl solution under static (S) and dynamic (D) electrolyte conditions, respectively. The following electrochemical test methods were used in this work: electrochemical impedance spectroscopy (EIS), potentiodynamic polarization (PD), potentiostatic polarization (PS), and the Mott-Schottky (MS) test. The EIS measurements were carried out at an AC amplitude of 10 mV in the frequency range of 10<sup>4</sup> Hz to 10<sup>-2</sup> Hz after a stable open circuit potential (OCP) value being obtained. The EIS results were analyzed using *ZsimpWin* software. The PD tests were performed between the potential of -0.25 V (vs. OCP) and 2 V with a scan rate of 0.1667 mV s<sup>-1</sup>. Based on the passivation potential range measured in the PD test, the potentials of 0.6, 0.9, 1.1, 1.3, and 1.5 V were separately selected to perform a 2 h PS test to produce an oxide film on the sample surface. After PS treatment, EIS was re-measured to obtain an effective capacitance of the produced oxide film. Afterward, MS measurements were performed using a 10 mV AC signal and a step rate of 50 mV s<sup>-1</sup> at 1000 Hz to investigate the semiconductive properties of the produced oxide film. At least three parallel experiments were conducted in this work to ensure data reproducibility.

### 2.3. Microstructural characterizations

The phase constituent of the SLMed Ti-6Al-4V alloy was determined using X-ray diffraction (XRD) equipped with a PANalytical Empyrean diffractometer with Cu-K<sub>α</sub> radiation. The scanning range was set at the 2θ angle between 30° and 80° with a scanning rate of 0.03 ° s<sup>-1</sup>. The XRD results were analyzed by *HighScore* software using the *PAN-ICSD* database. The surface morphologies of the samples before and after corrosion were characterized by a dual-beam field-emission scanning electron microscope (SEM) with a focused ion beam milling system (FIB-SEM, Helios NanoLab G3 CX, FEI), the FIB-SEM was also coupled with an Oxford Instruments X-Max 80 energy dispersive X-ray spectrometer (EDS). The longitudinal sections of the oxide films formed on the SLMed Ti-6Al-4V alloys after PD for all test conditions were prepared by FIB milling, and the FIB-milled wafers were analyzed by a transmission electron microscopy (TEM, Titan G2 80–200, FEI). In addition, the surface of the alloy was pre-deposited with a thin layer of Au in a Smart Coater (JEOL) to improve the conductivity on the surface prior to the SEM and to protect the sample surface from any damage during the FIB

milling, and a section of  $2\ \mu\text{m} \times 15\ \mu\text{m}$  of each sample was selected to deposit a thick C layer in FIB-SEM chamber to provide extra protection on the sample surface. The wafers were further thinned by the ion beam with lower currents for investigation of its oxide film in TEM. The formed oxide films after PD for all test conditions were also subject to an X-ray photoelectron spectrometer (XPS, ESCALAB 250, Thermo VG) surface analysis system with a monochromatic Al  $K_{\alpha}$  X-ray source of 1486.6 eV. The diameter of the beam spot was 400  $\mu\text{m}$ , the take-off angle was 90°, the pass energy was 30 eV. The argon ion beam sputtering depth was chosen at 0 nm, 3 nm, and 10 nm with the sputtering rate of 0.1 nm  $\text{s}^{-1}$ . The Thermo Advantage software was used for the analysis of the XPS results. Furthermore, all prepared samples for microstructural characterizations were put in the drying cabinet and tested within 24 h to reduce the oxidation of the samples in the air.

### 3. Results

#### 3.1. Electrochemical measurements

Fig. 1 shows the EIS plots for the SLMed Ti-6Al-4V in the static and dynamic NaCl solutions with different NaCl concentrations. The Nyquist plots in Fig. 1(a) show a relatively large semi-circle for all test conditions. Generally, a larger radius of the semi-circle indicates a more

difficult electron transfer between the electrolyte and the tested material, which means that the Ti matrix in this work presents a better corrosion resistance [47]. However, it is difficult to distinguish the corrosion resistance of samples from Fig. 1(a) because the semi-circles for all conditions have a very close radius. The Bode phase angle plots reveal that the curves in the middle- to the high-frequency region under all conditions are in a platform shape (plateau level) and close to 90°, as shown in Fig. 1(b). This means that a compact oxide film forms on the sample surfaces [32,48]. Unlike the Nyquist plots, the plateau level from the Bode phase angle plots increases with an increase in the NaCl concentration, and the values of low-frequency phase angle has a decrease trend in the following sequence: S10/D10 ( $-76^\circ$ ) > S3.5/D3.5 ( $-71^\circ$ ) > S0.9/D0.9 ( $-66^\circ$ ). In addition, the phase angle in the low-frequency region presents a non-ideal capacitance behavior, and the impedance response in this region is predominantly controlled by the oxide film formed after a stable OCP reaches [49]. Therefore, the EIS results seem to be more closely related to the NaCl concentrations rather than to the electrolyte state.

To determine the capacitance of the oxide film formed on SLMed Ti-6Al-4V, the equivalent electrical circuit (EEC) was used to fit the EIS results. According to the Nyquist plots in Fig. 1, a single-time constant of EEC could be employed (Fig. 1(a) inset), and the fitting results are summarized in Table 1. The EEC used in Fig. 1(a) inset employs a CPE (constant phase element) component instead of the capacitance ( $C_{CPE}$ ) because the electrode surface (SLMed Ti-6Al-4V) is not ideally flat according to the uneven surface under microscopic level even the crystal plane is achieved after mechanical polishing (which is quite common scenario as widely reported in literature). Furthermore,  $n$  is the dispersion index and the value of  $n$  indicates the deviation from pure capacitor ( $n = 1$ ) [50]. The CPE is parallelly connected with an oxide film resistance ( $R_o$ ) and serially connected the previous two components with a solution resistance ( $R_s$ ). As shown in Table 1, the  $R_s$  gradually reduces with an increase in the NaCl concentration from 0.9–10 wt%, and the  $R_o$  changes oppositely. The results indicate that the higher concentration of NaCl solution promotes the conductivity of the electrolyte and the reactions between the substrate and electrolyte, hence a thick oxide film with higher  $R_o$  is suggested to be produced.

The EIS results that  $n$  approaches to 1 also confirm that the oxide films formed on all samples possess capacitive behavior. Hence, the oxide film could refer to a semiconductor with point defects (e.g., oxygen vacancies and metal interstitials) [51,52]. In order to investigate the film properties by MS analysis [23], a set of PS tests were conducted to produce oxide films under different electrolyte conditions. The PS

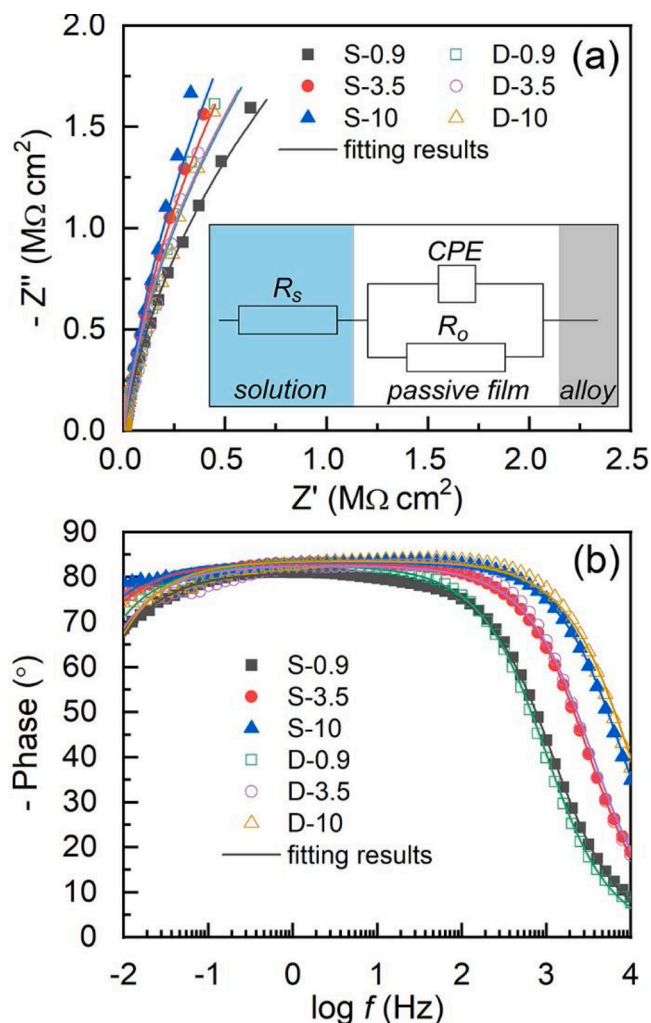


Fig. 1. EIS plots for SLMed Ti-6Al-4V in static and dynamic NaCl solutions with different concentrations: (a) Nyquist plots and (b) Bode plots. Inset in (a) is the equivalent electrical circuit used for fitting the EIS results. S and D indicate the static and dynamic electrolyte states, and 0.9, 3.5, and 10 are the concentrations (by weight percentage) of the NaCl solution, respectively.

Table 1

Summary of fitted EIS results in Fig. 2. The fitted solution resistance and the oxide film resistance are denoted by  $R_s$  and  $R_o$ , respectively. CPE and  $n$  represent the capacitor parameters respectively, which indicate the constant phase element and deviation degree of the capacitor.  $\chi^2$  indicates the fitting qualities. S and D indicate the static and dynamic electrolyte states, and 0.9, 3.5, and 10 are the concentrations (by weight percentage) of the NaCl solution, respectively.

Sample	$R_s$ ( $\Omega\ \text{cm}^2$ )	$CPE \times 10^5$ ( $\Omega^{-1}\ \text{cm}^{-2}\ \text{S}^n$ )	$n$	$R_o$ ( $\text{M}\Omega\ \text{cm}^2$ )	$\chi^2 \times 10^{-3}$
S-0.9	$52.39 \pm 0.86$	$1.69 \pm 0.16$	$0.91 \pm 0.009$	$6.60 \pm 0.45$	$0.9 \pm 0.5$
	$50.97 \pm 1.86$	$1.51 \pm 0.05$	$0.92 \pm 0.003$	$8.70 \pm 0.25$	$1.9 \pm 0.5$
D-0.9	$15.64 \pm 0.75$	$1.48 \pm 0.14$	$0.93 \pm 0.003$	$12.2 \pm 4.57$	$0.2 \pm 0.1$
	$14.26 \pm 0.37$	$1.44 \pm 0.09$	$0.92 \pm 0.003$	$7.57 \pm 1.05$	$3.2 \pm 0.5$
S-3.5	$6.23 \pm 0.48$	$1.34 \pm 0.09$	$0.93 \pm 0.002$	$24.3 \pm 17.4$	$0.4 \pm 0.3$
	$5.97 \pm 0.25$	$1.52 \pm 0.01$	$0.93 \pm 0.002$	$6.86 \pm 0.29$	$2.7 \pm 0.4$

potentials were chosen based on the passivation range measured in the PD curves.

Fig. 2(a) shows the PD curves for the SLMed Ti-6Al-4V in static and dynamic NaCl solutions with different concentrations. The PD curves of all samples are similar as evidenced by the almost overlapped curves shown in Fig. 2(a). The passivation current density is kept at  $\sim 0.6 \mu\text{A cm}^{-2}$  from  $\sim 0.5 \text{ V}$  to  $\sim 1.5 \text{ V}$  and increases slightly above the applied potential of  $1.5 \text{ V}$ . The slight increase in the current density above  $\sim 1.5 \text{ V}$  in Fig. 2(a) cannot indicate the pitting corrosion and breakdown of the generated oxide film, because Yang et al. [39] pointed out that the pitting potential (or breakdown potential) of SLMed Ti-6Al-4V takes place when the applied potential is greater than  $\sim 4 \text{ V}$ . Therefore, the increase in the current density after  $\sim 1.5 \text{ V}$  only illustrates that the formed oxide films are unstable and tend to be dissolved (Fig. 2(a)), or they are caused by the water decomposition on above  $\sim 1.3 \text{ V}$  [53]. Interestingly, the increase in the current density above  $\sim 1.5 \text{ V}$  is with the following sequence: S0.9/D0.9 > S3.5/D3.5 > S10/D10, as shown in Fig. 2(a) inset, which means that the higher NaCl concentration could prevent the increase in current density above  $\sim 1.5 \text{ V}$ . Nevertheless, all SLMed Ti-6Al-4V samples are still passivated.

The corrosion potential ( $E_{\text{corr}}$ ) and corrosion current density ( $i_{\text{corr}}$ ) in Fig. 2(a) were fitted using the XM-studio ECS software and the results are summarized in Fig. 2(b). The  $E_{\text{corr}}$  and  $i_{\text{corr}}$  have a downward trend with increasing the NaCl concentration. This indicates that the increased concentration of  $\text{Cl}^-$  directly affects the  $E_{\text{corr}}$  and makes corrosion easier to occur [54]. In addition, the sample has a higher  $E_{\text{corr}}$  in the static NaCl environment (for all test concentrations) than in the dynamic environment. In comparison, the change in the  $i_{\text{corr}}$  is reversed. Furthermore, according to Faraday's law [55], a higher  $i_{\text{corr}}$  value generally indicates a

higher corrosion rate of the sample. The  $i_{\text{corr}}$  is also related to the nature of the formed oxide film, such as the thickness, conductivity, and so on [56]. Therefore, the results from the PD curves demonstrate that the flowing electrolyte also affects the corrosion resistance of the SLMed Ti-6Al-4V, and the corresponding corrosion resistance in the dynamic environment increases.

### 3.2. Potentiostatic polarization

A series of film formation potentials (0.6, 0.9, 1.1, 1.3 and 1.5 V) have been selected according to the passivation range displayed in the PD curve (Fig. 2(a)) to produce oxide films. Fig. 3 shows the current-time curves in double logarithmic coordinates for the SLMed Ti-6Al-4V under different PS potentials. Fig. 3(a)–(f) indicate that all curves have almost the same trend and the current density still decreases linearly after 2 h PS. This proves the formation of a quasi-steady state of oxide film under all PS potentials [13]. Generally, the formation and dissolution of the oxide film simultaneously take place, so that a compact inner oxide layer and loose outer oxide layer could be formed on metal surface through metal dissolution, nucleation and growth mechanism under diffusion control [57,58]. The slopes of the curves in Fig. 3 (a)–(f) could specify the quality of the oxide films. It was reported that the formed oxide film is dense when the slope is close to  $-1$  while the oxide film becomes porous when the slope is close to  $-0.5$  [59]. The slopes of the curves under all conditions have been fitted and are also summarized in Fig. 3(a)–(f). The results indicate that the compact oxide film is most likely to form under the PS potential of 0.6, 0.9 and 1.1 V, and the porous oxide film is most likely to form under the PS potential of 1.3 and 1.5 V. Fig. 3(g) and (h) are the fitted current densities from the current-time curves (Fig. 3(a)–(f)) for the oxide film at quasi-steady state under different PS potentials. The curves display a similar trend that the current density gradually increases with increasing the PS potential for all test conditions. The fitted current densities are also very close under each applied PS potential, which indicates that the quasi-steady state oxide film could be formed under externally applied potential. Moreover, the nearly overlapped curves in Fig. 3(g) and (h) indicate that the quasi-steady state current density for the formed oxide film at a quasi-steady state is not closely related either to the concentration of NaCl or to the electrolyte state.

### 3.3. Mott-Schottky measurements

Fig. 4 shows the MS curves of potentiostatic polarized samples in the NaCl solutions with different concentrations and different electrolyte states. Generally, the oxide films formed on SLMed Ti-6Al-4V alloy samples demonstrate a typical  $n$ -type semiconductive behavior [60], which could be confirmed from the positive slopes in the potential range between  $-0.8 \text{ V}$  and  $-0.6 \text{ V}$  (Fig. 4). The oxide film with  $n$ -type semiconductive properties usually contains oxygen vacancies and/or cation interstitials (donors) [52]. The donor densities ( $N_D$ ) of the oxide film could be calculated from the slopes of the MS curves. The slope is equal to  $\frac{2}{e\epsilon_0 e N_D}$  based on the  $n$ -type semiconductive MS expressions [18], where  $e$  is the electron charge ( $1.6 \times 10^{-19} \text{ C}$ ),  $\epsilon$  is the dielectric constant of the oxide film (e.g.,  $\text{TiO}_2$  is equal to 60 [60]), and  $\epsilon_0$  is the vacuum permittivity constant ( $8.85 \times 10^{-14} \text{ F cm}^{-1}$ ). Furthermore, as shown in Fig. 4, the capacitance value increases with the increase in the NaCl concentration for both static and dynamic conditions. Therefore, the related film thickness (or the ability of the oxide film in the carrying capacity of charge) [61,62] for the oxide film formed on the SLMed Ti-6Al-4V surface would be largely related to the NaCl concentration.

The calculated  $N_D$  for all SLMed Ti-6Al-4V alloy samples under different conditions is plotted in Fig. 5(a), (d) and (g). In general, a higher  $N_D$  value indicates a higher conductivity therefore a lower quality of oxide film with  $n$ -type semiconductive properties [60]. Apparently,  $N_D$  values have the same change trend for the samples under all

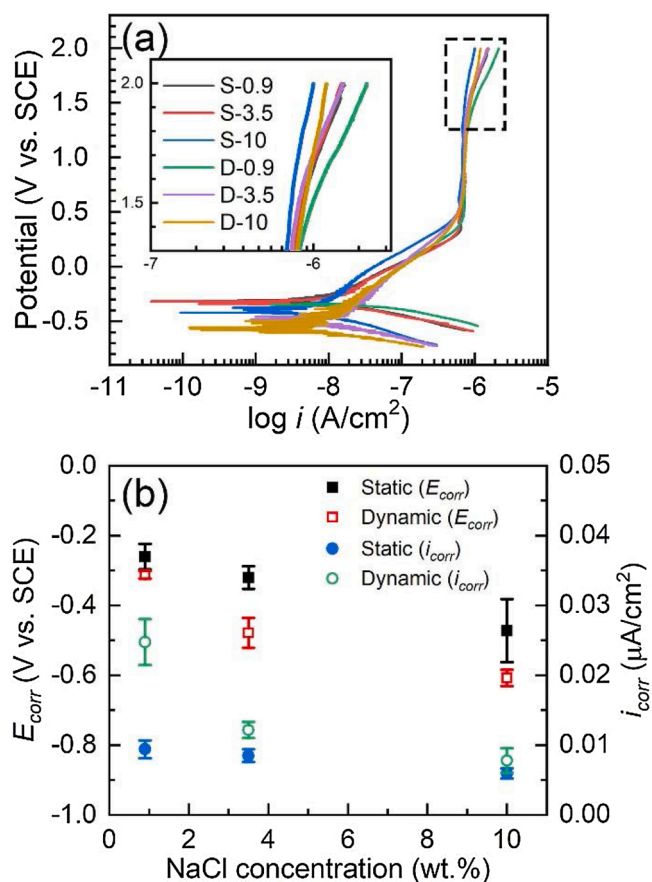


Fig. 2. (a) Potentiodynamic polarization curves for SLMed Ti-6Al-4V in the static and dynamic NaCl solutions with different concentrations; (b) fitted results of the corrosion potential ( $E_{\text{corr}}$ ) and corrosion current density ( $i_{\text{corr}}$ ) versus the concentration of NaCl solution.

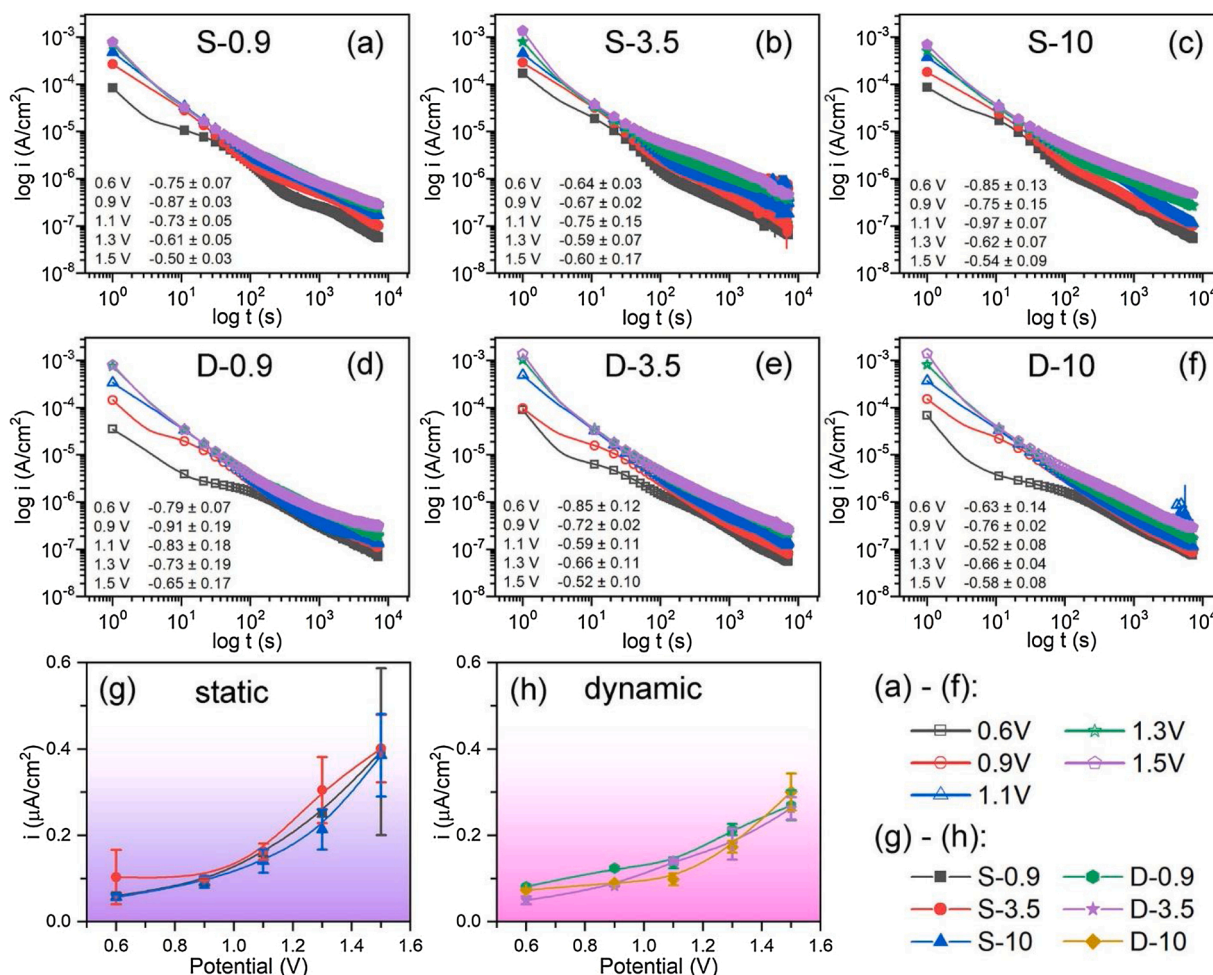


Fig. 3. Current-time curves in double logarithmic coordinates for SLMed Ti-6Al-4V under different potentiostatic polarization potentials (0.6, 0.9, 1.1, 1.3 and 1.5 V) for 2 h in the static and dynamic NaCl solutions with different concentrations: (a)-(c) the oxide film formed in the static electrolyte and (d)-(f) in the dynamic electrolyte; (g) and (h) are the fitted current densities for the formed oxide film at quasi-steady state under the conditions of static and dynamic electrolytes under different film formation potentials.

conditions:  $N_D$  gradually decreases with an increase in the film formation potential. Meanwhile, the average  $N_D$  value is largely related to the NaCl concentration. The average  $N_D$  increases with an increase in the NaCl concentration, indicating the quality of the formed oxide film decreases with an increase in the NaCl concentration.

The thickness ( $L_{SS}$ ) of the oxide film formed by PS can be also calculated using the following equation [60]:

$$L_{SS} = \frac{\epsilon \epsilon_0 A}{C_{eff}} \tag{1}$$

where  $A$  is the effective area of the electrode, and  $C_{eff}$  is the effective capacitance measured from EIS (at the frequency of 1000 Hz) after the production of the oxide film. The calculated values of  $L_{SS}$  are plotted in Fig. 5(b), (e), and (h); the results reveal that  $L_{SS}$  is largely related to the NaCl concentration.  $L_{SS}$  decreases as the NaCl concentration increases under all test conditions, which demonstrates the high concentration of NaCl solution is not beneficial for forming the oxide film. However, the electrolyte state may have little influence on the  $L_{SS}$ .

The growth kinetics of the oxide film formed on SLMed Ti-6Al-4V is determined by the diffusion coefficient ( $D_O$ ), which can be expressed by the following equation [60]:

$$D_o = \frac{i_p RT}{4e F E_L \omega_2} \tag{2}$$

where  $i_p$  is the current density at steady state;  $R$  is the ideal gas constant

( $8.314 \text{ J mol}^{-1} \text{ K}^{-1}$ );  $T$  is the absolute temperature;  $e$  is the electron charge; and  $F$  is the Faraday's constant ( $96487 \text{ C eq}^{-1}$ ).  $\omega_2$  is the fitted constant in Fig. 5(a), (d) and (g) from the  $N_D$  expression [51].

$$N_D = \omega_1 e^{-bE_{FB}} + \omega_2 \tag{3}$$

$e_L$  is the electric field intensity, which is related to the applied potential and the film thickness (Fig. 5(b), (e) and (h)). Hence, their relationship is shown as [60]:

$$L_{SS} = \frac{(1 - \alpha)E}{e_L} + B \tag{4}$$

where  $\alpha$  is the surface polarizability with a value of 0.5 and  $B$  is a constant [63]. The calculated  $D_O$  values are also plotted in Fig. 5(c), (f) and (i). The results of  $D_O$  could refer to the growth kinetics of the formed oxide film that the increased value of  $D_O$  refers to easier oxygen vacancy diffusion across the oxide film and faster electrochemical reaction at the film/solution interface [50,64]. Overall, the corrosion resistance of the sample obtained in MS measurements is not consistent with the results in the electrochemical measurements discussed above (Figs. 1 and 2). Therefore, the analysis of the surface constitution is required to investigate the reasons.

### 3.4. Microstructural features

Fig. 6 shows the XRD patterns for the freshly polished SLMed Ti-6Al-

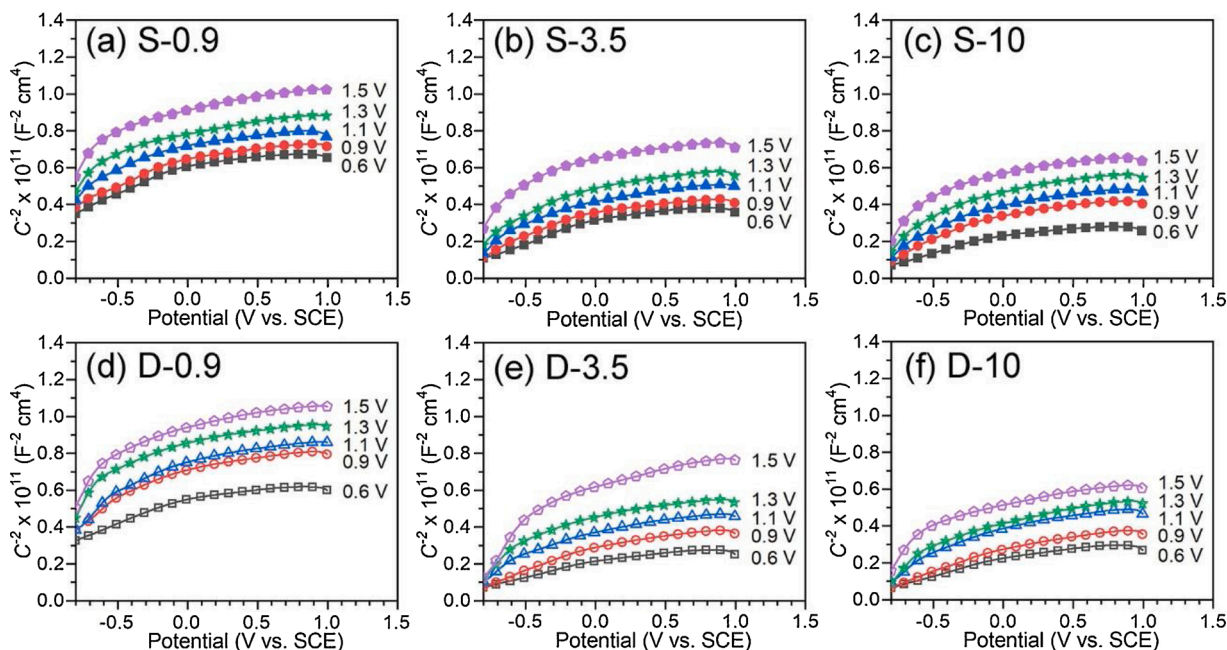


Fig. 4. Mott-Schottky curves of potentiostatically polarized samples under different conditions: (a)-(c) static and (d)-(f) dynamic NaCl solutions with the concentrations of 0.9, 3.5 and 10 wt%, respectively.

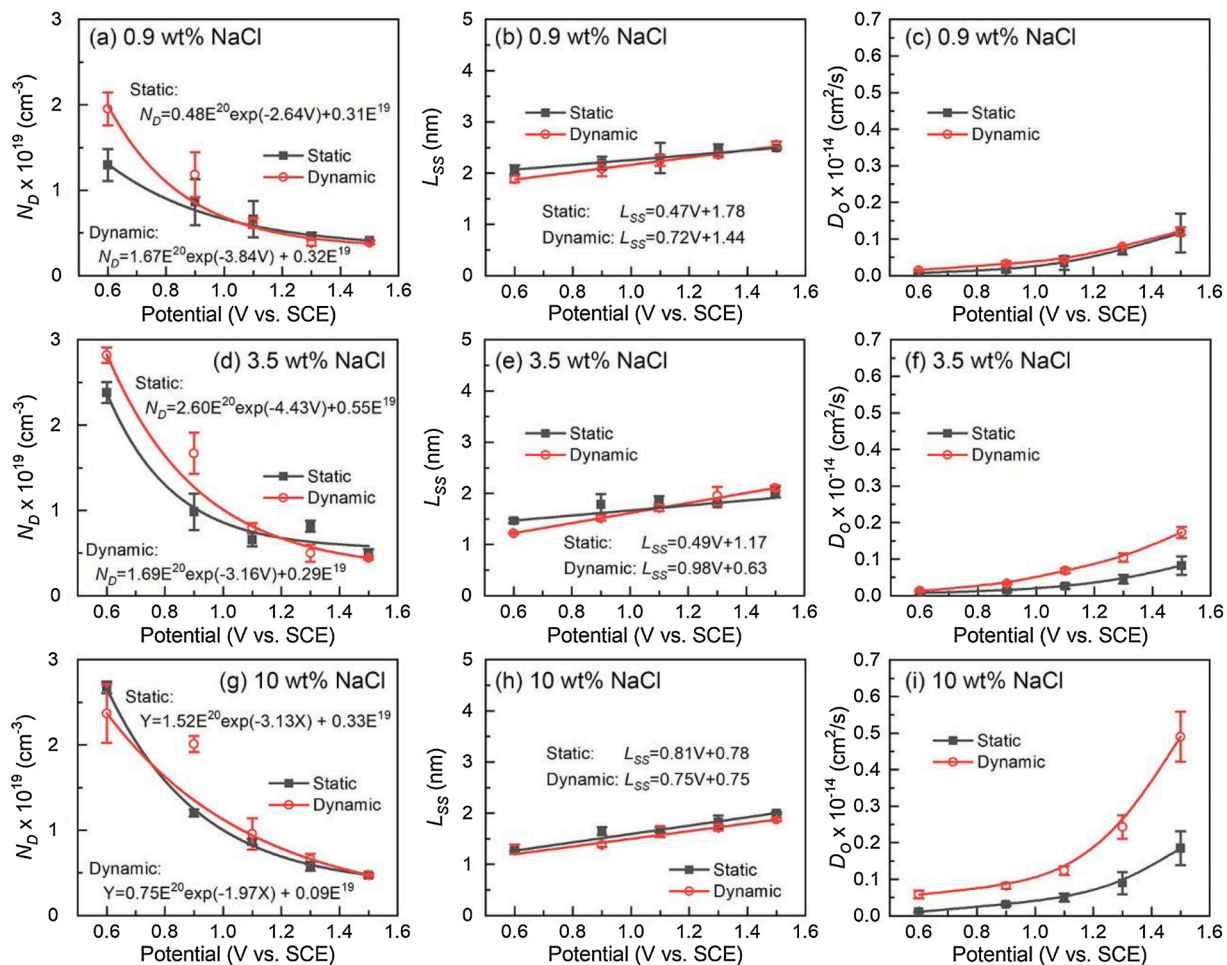


Fig. 5. Calculated donor densities ( $N_D$ ), oxide thicknesses ( $L_{SS}$ ), and vacancy diffusion coefficients ( $D_O$ ) of the oxide films formed on SLMed Ti-6Al-4V under different potentiostatic polarization potentials (0.6, 0.9, 1.1, 1.3 and 1.5 V) for 2 h in the static and dynamic NaCl solutions with different concentrations: (a)-(c) 0.9 wt%, (d)-(f) 3.5 wt%, and (g)-(i) 10 wt%.

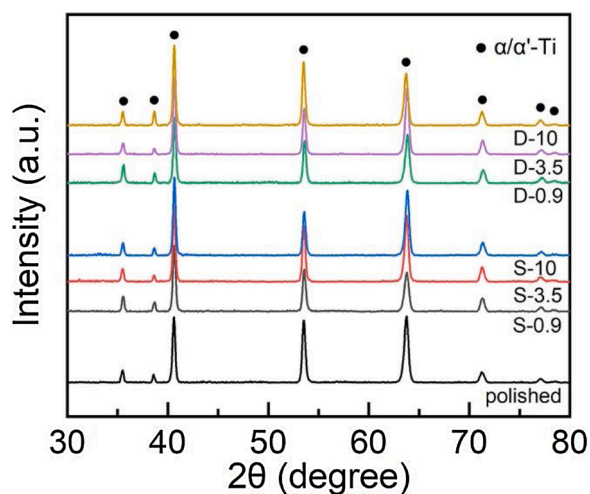


Fig. 6. XRD patterns for the SLMed Ti-6Al-4V and the ones after potentiodynamic polarization tests in the static and dynamic NaCl solutions with different concentrations, respectively.

4V samples (indicated as “polished” in Fig. 6) and those after PD tests in the static and dynamic NaCl solutions with different concentrations, respectively. All peaks shown in Fig. 6 are identified as  $\alpha/\alpha'$  Ti phase after matching with the *PAN-ICSD* database and literature [65,66], and there is no difference in phase constitution between various testing conditions (i.e. static and dynamic conditions) and different NaCl concentrations in this work. The XRD results indicate that no large quantities of corrosion products with new phases are generated after PD. Furthermore, the results also indicate that oxide film is not detected by XRD after PD since its significantly low thickness.

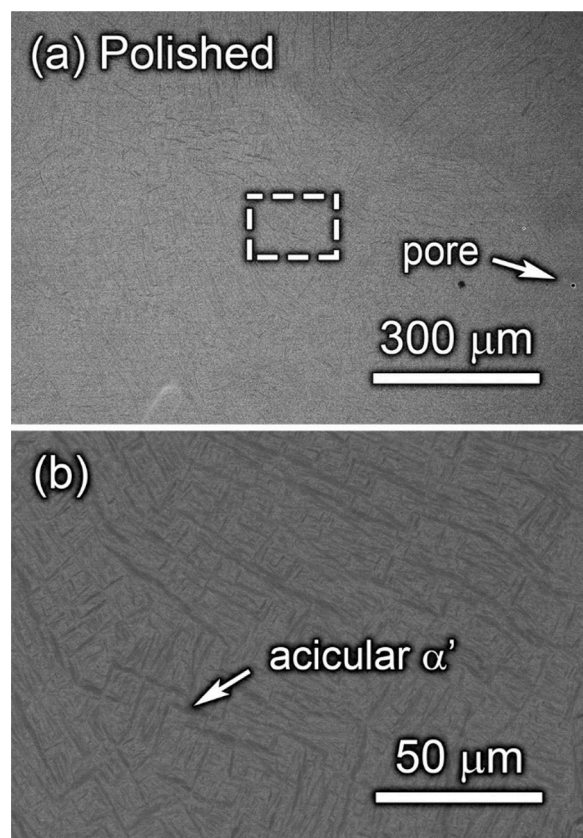
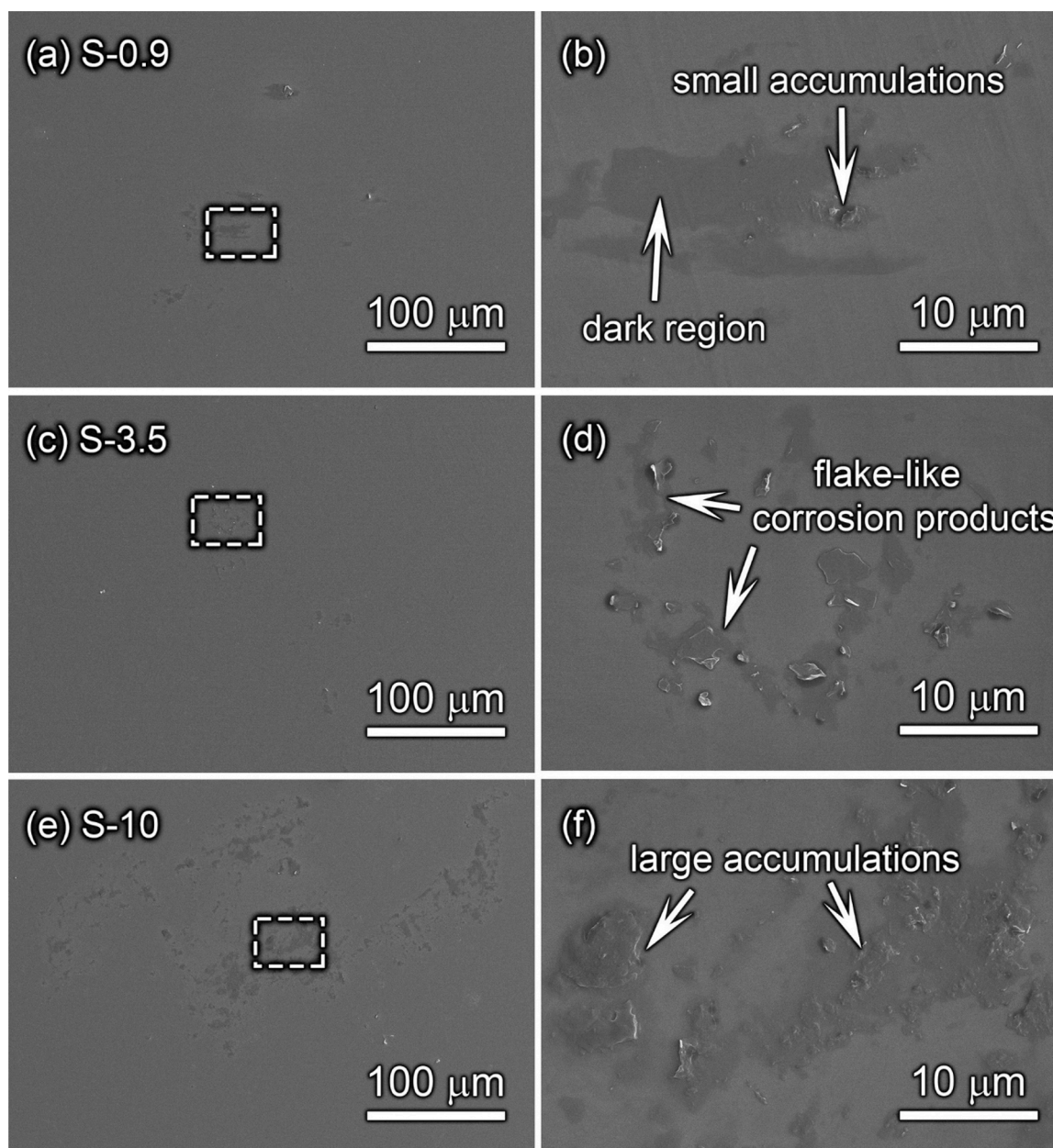


Fig. 7. SEM images of the (a) polished SLMed Ti-6Al-4V, and (b) an enlarged region in (a).

Fig. 7(a) shows the backscattered SEM image of the polished SLMed Ti-6Al-4V surface. In addition, Fig. 7(a) also presents some small spherical pores (defects) that result from the SLM manufacturing. Such defect pores cannot be eliminated during the SLM process. Laleh et al. [67] proposed that the shape of the defect pores produced by SLM are spherical and/or non-spherical (irregular). Generally, the spherical pores are smaller in size than the irregular ones [67]. The possible reasons causing the defect pores could include the improper SLM processing parameters, metal powder defects, balling, material vaporization, and/or imperfect collapse [68]. Fig. 7(b) is the enlarged image from Fig. 7(a) that indicates the microstructure of SLMed Ti-6Al-4V is mainly dominated by acicular  $\alpha'$  martensite [69], and the formation of acicular  $\alpha'$  martensite by non-diffusion phase transformation results from the rapid melting and solidification in the SLM process [70].

Fig. 8 shows the SEM images of the SLMed Ti-6Al-4V after PD in static conditions with different NaCl concentrations. In a relatively large macro-scale, it is difficult to find the distinct difference in corrosion morphology between 0.9 and 3.5 wt% NaCl solution after PD in the static electrolyte, as shown in Fig. 8(a) and (c). Apparently, the corrosion morphology for the alloy after PD in static condition with 10 wt% NaCl solution is apparently different from the former two counterparts (i.e. in 0.9 wt% and 3.5 wt% NaCl solutions). The detailed differences between them are shown in Fig. 8(b), (d), and (f), which are the enlarged regions from Fig. 8(a), (c) and (e) respectively. The common point of the corrosion morphology in Fig. 8(b), (d), and (f) is the formation of the dark region when corrosion takes place. The flake-like corrosion products are accumulated on top of the dark region and expand with an increase in the NaCl concentration. The corrosion products present in Fig. 8 seem to be the oxide film which is produced and peeled off from the Ti matrix, and the composition of the oxide film could be the mixture of  $\text{TiO}$ ,  $\text{Ti}_2\text{O}_3$ , and  $\text{TiO}_2$  [37,43,71]. In addition, the flake-like corrosion products grow from 2 μm in length (the maximum in Fig. 8 (b)) to 4 μm in length (the maximum in Fig. 8 (d)) with the NaCl concentration increases from 0.9 to 3.5 wt%. The morphology is also altered from small accumulations on the top of the dark regions to some large flakes covered on most of the whole dark region. The corrosion products further increase to 7 μm in length (the maximum in Fig. 8 (f)) under 10 wt% NaCl electrolyte test and such products cover most of the dark region with evidenced thickness, as shown in Fig. 8 (f). Therefore, the corrosion morphology shown in Fig. 8 indicates that the corrosion resistance of the SLMed Ti-6Al-4V is sensitive to the concentration of  $\text{Cl}^-$  in the electrolyte and the corrosion products are found to grow with the increase in the NaCl concentration. Furthermore, the phosphates would precipitate in the defects of SLMed Ti-6Al-4V in Hanks's solution [37] but were not presented in NaCl solution in the current work. Therefore, the negative effect of the defects on corrosion for the SLMed Ti-6Al-4V can be neglected in this work.

Fig. 9 shows the SEM images of the SLMed Ti-6Al-4V after PD in the dynamic NaCl solutions with different concentrations. Similar to the results in the static condition (Fig. 8), the regions affected by corrosion increase with increasing the NaCl concentration, as shown in Fig. 9(a), (c) and (d). However, the size of the corrosion products has an opposite change trend compared to those of the alloys tested under static conditions; the corrosion products decrease from 12 μm in length (the maximum length in Fig. 9(b)) to 10 μm in length (the maximum length in Fig. 9(d)) with the NaCl concentration increase from 0.9 wt% to 3.5 wt%. The corrosion morphology is also changed from large flake-like accumulations to relatively small corrosion products. The size of corrosion products further decreases to 4 μm (the maximum in Fig. 9(f)) in the 10 wt% NaCl electrolyte tests. However, the quantities of the corrosion products increase compared to the corrosion products formed in 0.9 wt% to 3.5 wt% NaCl solution, as shown in Fig. 9(f). Although the size of the corrosion products decreases with an increase in the NaCl concentration (Fig. 9(b), (d) and (f)), the region affected by corrosion increases after PD (Fig. 9(a), (c) and (e)). Therefore, the corrosion morphology, as shown in Fig. 9, still suggests a declined corrosion



**Fig. 8.** SEM images of the SLMed Ti-6Al-4V after potentiodynamic polarization tests in the static NaCl solutions with the concentrations of: (a) 0.9 wt%, (c) 3.5 wt%, and (e) 10 wt%; (b), (d) and (f) are the enlarged regions from (a), (c) and (e), respectively.

resistance of the alloys with increased NaCl concentration under dynamic electrolyte conditions based on the SEM observations. However, the corrosion products or the accumulations detected in SEM images (Figs. 8 and 9) cannot describe the morphology of the oxide film in detail as the SEM images are only the top view of the sample surface. Therefore, the cross-sectional characterization of the sample is needed to investigate the thickness and quality of the produced oxide film.

### 3.5. Oxide film features

In order to obtain a practical thickness of the oxide film, high-angle annular dark-field (HAADF) scanning TEM images with corresponding EDS analysis (cross-sectional view) of SLMed Ti-6Al-4V samples after PD tests are shown in Figs. 10 and 11, respectively. The oxide films formed in the static condition (Fig. 10) prominently covered on the sample surface between the Ti-matrix and Au depositions. Interestingly, the thickness of the oxide film increases from  $\sim 10.6$  nm in 0.9 wt% NaCl

solution to  $\sim 11.2$  nm in 3.5 wt% NaCl solution, and the thickness of the oxide film further increases to  $\sim 12.5$  nm in 10 wt% NaCl solution. The change in thickness of the oxide film after PD is inconsistent with the calculated thickness of the oxide film after PS under a wide potential range. The reason for the increased oxide film thickness with an increase in the NaCl concentration could be that only  $\text{TiO}_2$  was considered as the main content of the oxide film during the theoretical calculation [60]. However, the components of the oxide film formed on the Ti alloy surface may include  $\text{TiO}$ ,  $\text{Ti}_2\text{O}_3$ , and  $\text{TiO}_2$  [43]. During the formation process of the oxide film on the Ti alloy surface,  $\text{TiO}$  and  $\text{Ti}_2\text{O}_3$  continue to form and partially transform into the highest valence oxides ( $\text{TiO}_2$ ) [43, 46]. Because high-concentration NaCl could promote the reactions (with lower  $R_s$ ) between metal and electrolyte, and the halide ion ( $\text{Cl}^-$ ) also has a positive effect on corrosion [41]. Therefore, the formation of the  $\text{TiO}_2$  in the outmost layer would be inhibited in a high-concentration NaCl solution.

Similarly, the oxide film also forms on the sample surface under

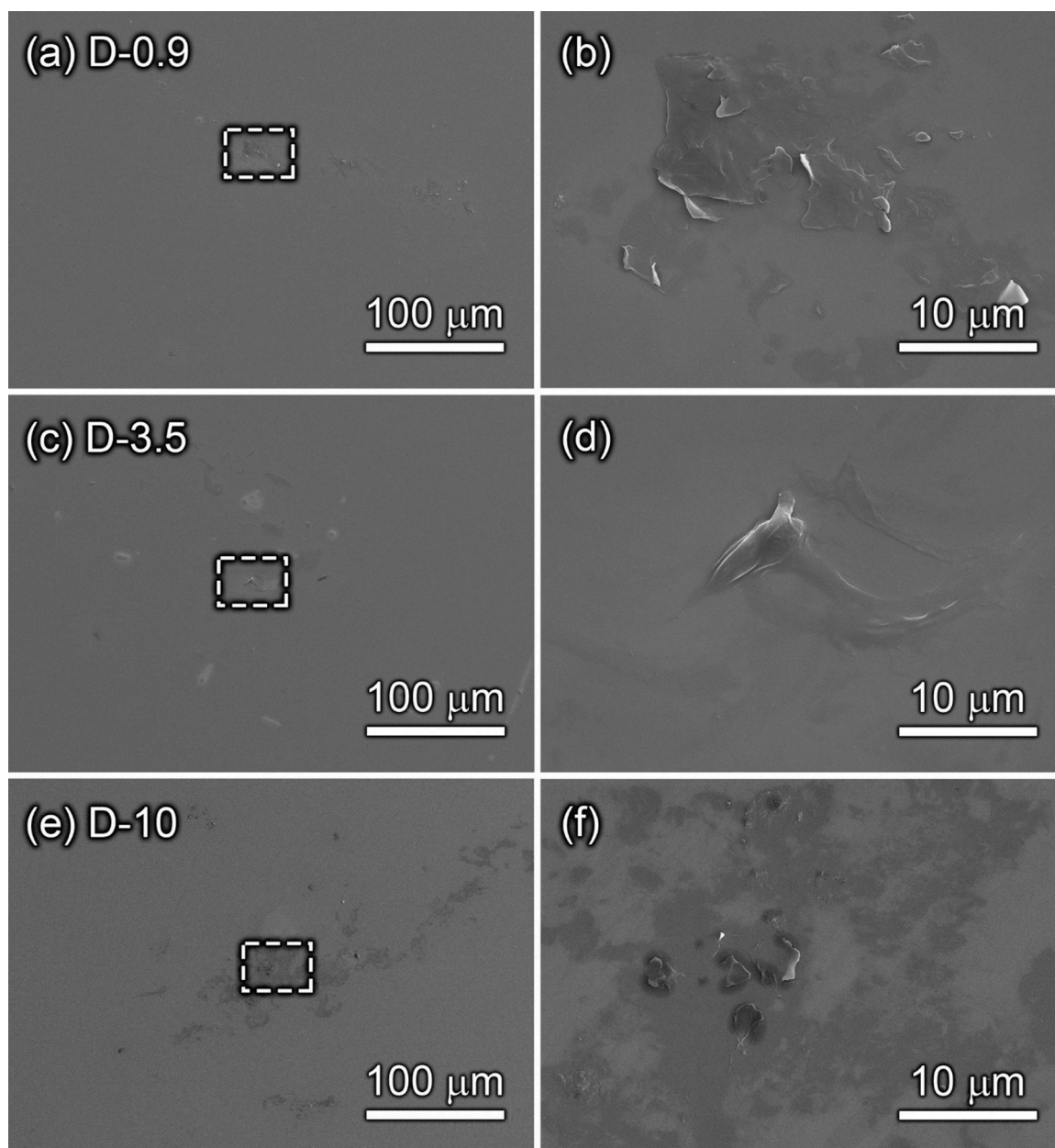


**Fig. 9.** SEM images of the SLMed Ti-6Al-4V after potentiodynamic polarization tests in the dynamic NaCl solutions with the concentrations of: (a) 0.9 wt%, (c) 3.5 wt %, and (e) 10 wt%; (b), (d) and (f) are the enlarged regions from (a), (c) and (e), respectively.

dynamic conditions, and the thickness change of the oxide film after PD is also inconsistent with the calculated thickness of the oxide film after PS under a wide potential range, as shown in Fig. 11. The thickness of the oxide film increases from  $\sim 10.6$  nm in 0.9 wt% NaCl solution to  $\sim 11.1$  nm in 3.5 wt% NaCl solution, and the thickness of the oxide film further increases to  $\sim 12.1$  nm in 10 wt% NaCl solution. Compared with the thickness of the oxide film measured in Fig. 10, the values of the thickness of the oxide film under dynamic conditions are slightly restrained than the corresponding ones in the static conditions. The corrosion of a metal is an actual material loss either by the dissolution of the material or by the formation of nonmetallic scales [72], and also the formation and dissolution of the oxide film simultaneously take place [15,58]. Therefore, a higher growth rate of the oxide film would have a higher thickness and the corrosion of the material is more severe.

The SLMed Ti-6Al-4V samples after PD tests in dynamic conditions with the NaCl concentration of 10 wt% were chosen to investigate the characteristics of the produced oxide film by TEM, and the results are

shown in Fig. 12. Fig. 12(a) shows a single layer of the oxide film, between the Ti matrix and the deposits, formed on the sample surface. The corresponding selected area electron diffraction (SAED) pattern of the Ti matrix shown in Fig. 12(b) inset indicates that the crystal structure of SLMed Ti-6Al-4V has a hexagonal structure.

To obtain the detailed and quantitative composition of the oxide film, the alloys are separately sputtered by  $\text{Ar}^+$  ion beam with different sputtering depths using XPS. The sputtering depth of 0 nm, 3 nm, and 10 nm are chosen for XPS analysis after considering the EDS analysis from Figs. 10 and 11, and the results are summarized in Figs. 13–15. The Ti 2p spectra in Figs. 13 and 14 are deconvoluted into three sets of doublet peaks corresponding to  $\text{Ti}^{4+}$ ,  $\text{Ti}^{3+}$ , and  $\text{Ti}^{2+}$ , which confirms the presence of the oxide of  $\text{TiO}_2$ , and the suboxides of  $\text{TiO}$  and  $\text{Ti}_2\text{O}_3$ . The locations of the three sets of doublet peaks are at the binding energies of  $459.0 \pm 0.3$  eV and  $465.0 \pm 0.3$  eV,  $457.5 \pm 0.1$  eV and  $463.4 \pm 0.2$  eV, and  $455.2 \pm 0.1$  eV and  $461.4 \pm 0.3$  eV, respectively.

Fig. 13 is the XPS spectra of the Ti 2p region for SLMed Ti-6Al-4V

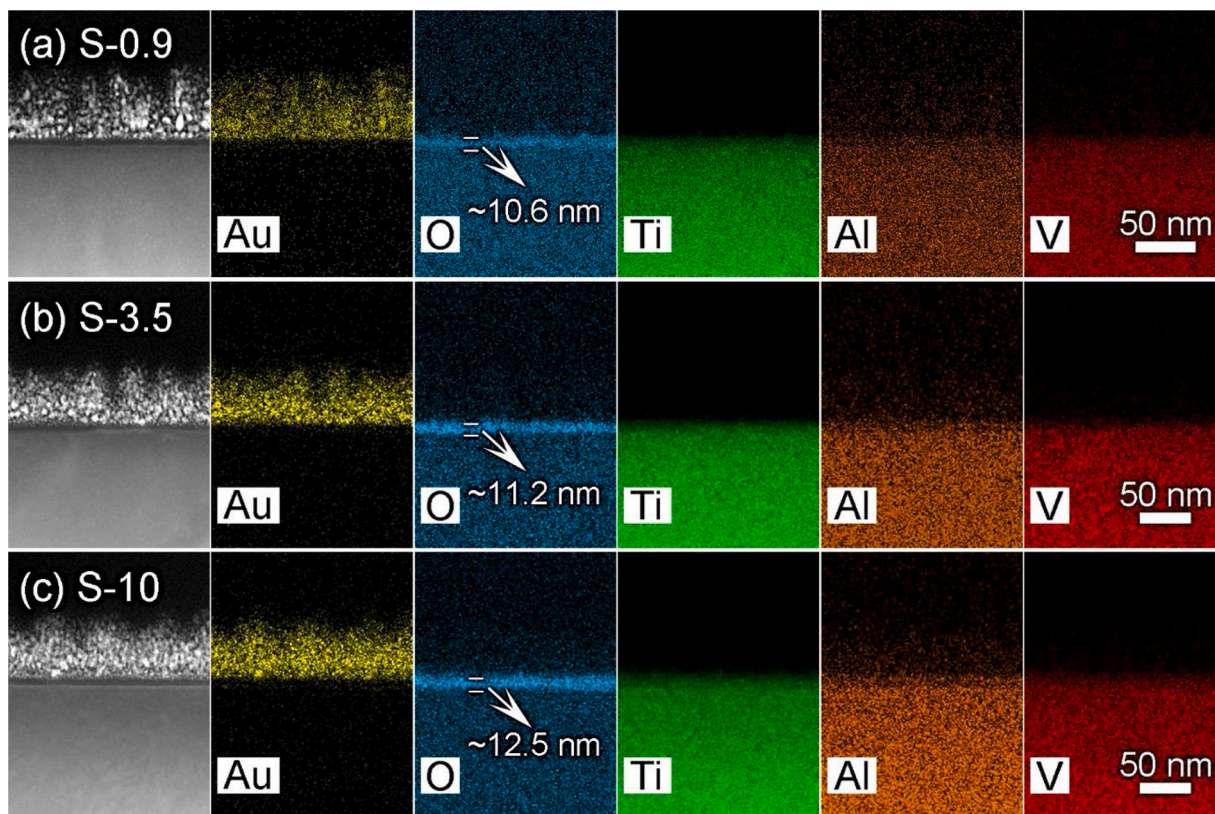


Fig. 10. High-angle annular dark-field (HAADF) scanning TEM images (cross-sectional view) of SLMed Ti-6Al-4V after potentiodynamic polarization tests in the static NaCl solutions with the concentrations of: (a) 0.9 wt%, (b) 3.5 wt%, and (c) 10 wt%, respectively.

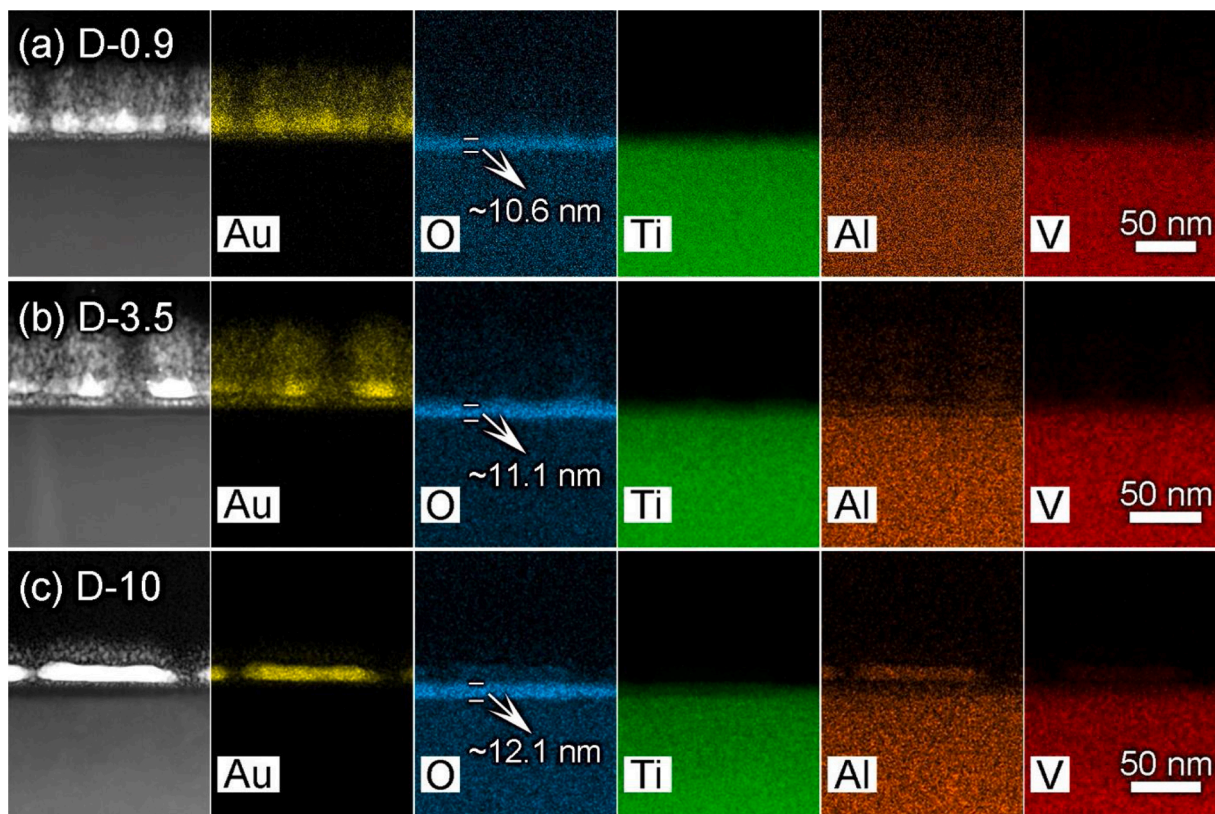
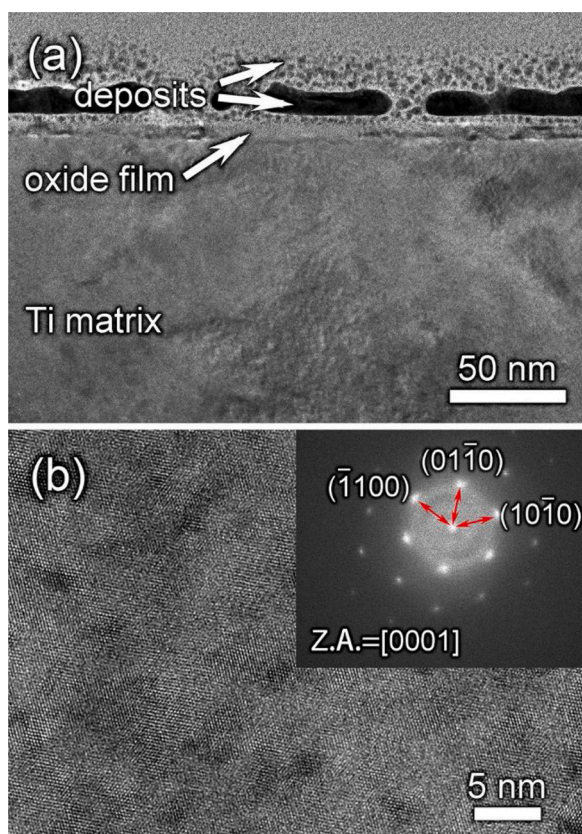


Fig. 11. High-angle annular dark-field (HAADF) scanning TEM images (cross-sectional view) of SLMed Ti-6Al-4V after potentiodynamic polarization tests in the dynamic NaCl solutions with the concentrations of: (a) 0.9 wt%, (b) 3.5 wt%, and (c) 10 wt%, respectively.



**Fig. 12.** (a) Bright-field TEM image of SLMed Ti-6Al-4V after potentiodynamic polarization tests in dynamic conditions with the NaCl concentration of 10 wt%, and (b) a high-resolution TEM image and its selected area electron diffraction (inset) of the Ti matrix.

after PD tests in the static NaCl conditions with the NaCl concentrations of 0.9, 3.5, and 10 wt%. Fig. 13 shows that the content of TiO<sub>2</sub> reaches the maximum value at the outmost layer from Fig. 13(a) to (c), and decreases with increasing the sputtering depth. By contrast, the contents of TiO and Ti<sub>2</sub>O<sub>3</sub> increase as the sputtering depth increases. According to Gebert et al. [43], TiO and Ti<sub>2</sub>O<sub>3</sub> continuously form on the Ti alloy surface in the initial growth stage and partially transform into the highest valence oxides TiO<sub>2</sub>. Therefore, the new existence of TiO in Fig. 13(c) reveals that the high concentration of NaCl solution suppresses the production of TiO<sub>2</sub>, as shown in Fig. 13(a)-(c). Actually, the suppression process could be defined as the concentrated NaCl electrolyte that promotes the transformation of TiO<sub>2</sub> from TiO and Ti<sub>2</sub>O<sub>3</sub>. But the aggressive nature of halide ions (e.g., Cl<sup>-</sup>) could dissolve the formed TiO<sub>2</sub>, especially in the electrolyte with high Cl<sup>-</sup> concentration. Therefore, the contents of TiO<sub>2</sub> decrease with an increase in the NaCl concentration. After the oxide film was sputtered 3 nm, the contents of Ti<sub>2</sub>O<sub>3</sub> increase in the oxide film formed in all different concentrations of NaCl solutions, which means that the Ti<sub>2</sub>O<sub>3</sub> is mainly concentrated at the central region of the oxide film. The content of TiO begins to increase with the sputtering depth to 10 nm; the less amount of TiO in Fig. 13(i) could suggest that oxide film with a high thickness forms on the S-10 sample and corresponds to the EDS results in Fig. 10.

Similarly, Fig. 14 is the XPS spectra of Ti 2p region for SLMed Ti-6Al-4V after PD tests in dynamic conditions with the NaCl concentration of 0.9, 3.5, and 10 wt%, respectively. The oxide composition of TiO<sub>2</sub> also reaches the maximum value at the outmost layer. The new existence of TiO in Fig. 14(c) indicates the high concentration of NaCl solution also suppresses the production of TiO<sub>2</sub> under dynamic conditions, as shown in Fig. 14(a)-(c). The Ti<sub>2</sub>O<sub>3</sub> is still concentrated at the central region of the oxide film but with less concentration in the sputtering depth of 3

nm, and the composition of TiO starts to increase when the sputtering depth was close to the Ti matrix. Fig. 14(h) and (i) could also suggest the oxide film with a higher thickness formed on the sample surface under dynamic 3.5 and 10 wt% NaCl solutions, which correspond to the EDS analysis in Fig. 11.

Fig. 15 summarizes the composition distribution of TiO<sub>2</sub>, Ti<sub>2</sub>O<sub>3</sub>, and TiO in Figs. 13 and 14. Compared with the thickness measured in Figs. 10(a) and 11 (a), the thickness of the oxide film formed in 0.9 wt% NaCl solution under static and dynamic conditions mainly depends on the contents of TiO<sub>2</sub> and TiO, as shown in Fig. 15(a) and (b). In the overall sputtering depth of 10 nm in 0.9 wt% NaCl solution, the fraction of TiO<sub>2</sub> decreases from 81% to 20% under static conditions, and from 81% to 33% under dynamic conditions. The fraction of TiO increases from 0% to 34% under static conditions and from 0% to 31% under dynamic conditions. The 3% difference in the contribution of TiO can be negligible compared to the 13% difference in the contribution of TiO<sub>2</sub>. Therefore, the 13% difference in the contribution of TiO<sub>2</sub> (with the same oxide film thickness) indicates that the oxide film formed in dynamic electrolyte has a more complete transformation of TiO<sub>2</sub> from TiO and Ti<sub>2</sub>O<sub>3</sub> in 0.9 wt% NaCl solution. This rule is also applied in 3.5 wt% NaCl solution and 10 wt% NaCl solution because a higher content of TiO<sub>2</sub> is present in the oxide film with a slightly lower thickness formed under the dynamic condition than that in the oxide film under the static condition.

In Fig. 15(a), (c), and (e), the fraction of TiO<sub>2</sub> decreases from 81% to 20% under 0.9 wt% NaCl solution, from 82% to 35% under 3.5 wt% NaCl solution, and from 55% to 38% under 10 wt% NaCl solution. Therefore, the fraction of TiO<sub>2</sub> decreases by 61% in 0.9 wt% NaCl solution to 47% in 3.5 wt% NaCl solution, and further decreases to 17% in 10 wt% NaCl solution and the decrement in the TiO<sub>2</sub> is also inconsistent with the increase in the total of Ti<sub>2</sub>O<sub>3</sub> and TiO. Therefore, the change of the oxide film thickness with increasing the NaCl concentration in Fig. 10 could be attributed to that the high concentration of Cl<sup>-</sup> promotes the transformation from Ti<sub>2</sub>O<sub>3</sub> and TiO to TiO<sub>2</sub>. Followed by the dissolution of the formed TiO<sub>2</sub> according to the aggressive properties of halide ions (e.g., Cl<sup>-</sup>) in the electrolyte. Therefore, the oxide film with a higher thickness and less corrosion resistance is formed in concentrated NaCl solutions (Fig. 2). A similar condition is also applied for the tests under dynamic conditions, as shown in Fig. 15 (b), (d), and (f). The fraction of TiO<sub>2</sub> decreases from 81% to 33% under 0.9 wt% NaCl solution, from 79% to 57% under 3.5 wt% NaCl solution, and from 69% to 44% under 10 wt% NaCl solution. The less decrement in the TiO<sub>2</sub> could attribute to the dynamic condition that promotes the transformation from Ti<sub>2</sub>O<sub>3</sub> and TiO to TiO<sub>2</sub>.

## 4. Discussion

### 4.1. Formation of the oxide film

According to the XPS analysis of the Ti 2p region from Figs. 13–15, TiO<sub>2</sub>, Ti<sub>2</sub>O<sub>3</sub>, and TiO in the oxide films are gradually presented as the major constituents from the outer side of the oxide layer to its inner side, which is consistent with the results in Hanawa's work [44]. The formation process could be described as the followings: at the very beginning of corrosion, TiO forms on Ti alloys surface and is immediately oxidized to its trivalence state (Ti<sub>2</sub>O<sub>3</sub>) to start the dehydration process, as shown in Eq. (5). The formed Ti<sub>2</sub>O<sub>3</sub> would transform to its tetravalence state (TiO(OH)<sub>2</sub>) before dehydration, as shown in Eq. (6). Finally, the most stable oxide (TiO<sub>2</sub>) is formed by the dehydration of TiO(OH)<sub>2</sub>, as shown in Eq. (7) [44–46]. The above-described processes are summarized below:

(a) Oxidation in the initial stage:



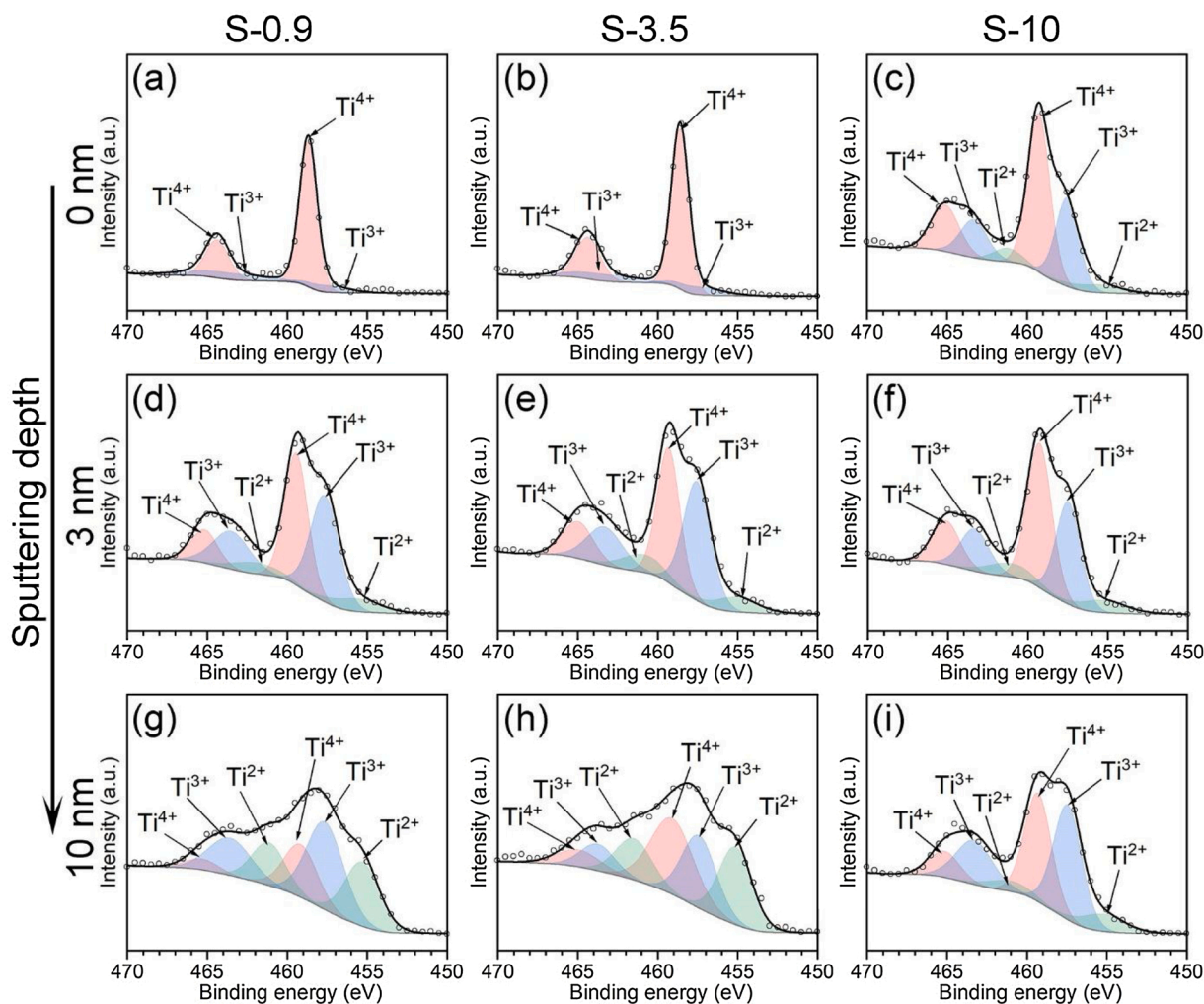
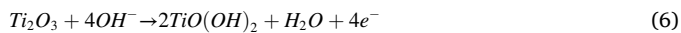


Fig. 13. XPS spectrum of Ti 2p region for SLMed Ti-6Al-4V after potentiodynamic polarization tests in static condition with the NaCl concentrations of 0.9, 3.5, and 10 wt%, respectively.

(b) Oxidation of TiO to its tetravalence:



(c) Dehydration:



According to the XPS results (Fig. 15),  $\text{TiO}_2$  is mainly distributed at the outermost surface of the oxide film. This means that the dehydration process only proceeds from the outermost surface of the oxide film, and the formation of  $\text{TiO}_2$  is inhibited according to the aggressive properties of halide ions (e.g.,  $\text{Cl}^-$ ) [41]. The dynamic equilibrium of the formation and dissolution of the oxide film is also obtained [57,58]. Meanwhile,  $\text{TiO}$  and  $\text{Ti}_2\text{O}_3$  would be continuously produced at the metal/film interface by the diffusion of O; therefore, the  $\text{TiO}$  and  $\text{Ti}_2\text{O}_3$  are dominated in the interior of oxide film. Furthermore, the presence of  $\text{Cl}^-$  in the electrolyte can accelerate the formation of oxide film; therefore, the material surface is quickly covered by oxide film (or corrosion products) [73,74]. In this process,  $\text{Cl}^-$  would compete with  $\text{OH}^-$  to adsorb on the oxide surface and be exposed to the defect sites on the oxide film [75]. The local thinner (corrosion) of the oxide film would be accelerated by reducing the activation energy of metal cation transfer [76]. For the SLMed Ti-6Al-4V investigated in this work, the oxide film formed on the sample surface continues to thicken with the increase in the  $\text{Cl}^-$  concentration. However, the thickness of the formed oxide film under the

dynamic conditions declines slightly in the same  $\text{Cl}^-$  concentration. The reason could be attributed to that the passivation is slowed down under the dynamic condition by the insufficient supply of  $\text{OH}^-$  (high concentration of  $\text{Cl}^-$ ), which promotes the transformation of  $\text{TiO}_2$  from  $\text{TiO}$  and  $\text{Ti}_2\text{O}_3$  during the corrosion process.

#### 4.2. Effect of NaCl concentration on corrosion

According to the EIS results in Table 1, the  $R_s$  decreases with an increased concentration in the NaCl solution. The decreased  $R_s$  suggests a faster charge transfer therefore easier occurrence of the reaction between metal and electrolyte. The fitted  $R_o$  from EIS results indicates the resistance of the sample after 2 h immersion increases in the following sequence for the sample tests in static condition:  $S0.9 < S3.5 < S10$ . Therefore, the faster charge transfer and easier occurrences of the reaction between metal and electrolyte could lead to a thick oxide film formed in the high concentration of NaCl (Figs. 10 and 11). Furthermore, a similar value of  $R_o$  is obtained for the sample tests in dynamic condition because the dynamic condition promotes the dissolution of the formed oxide ( $\text{TiO}_2$ , outer side of the oxide film) by the aggressive properties of  $\text{Cl}^-$ . However, the phase angle (the plateau level in the middle-frequency range) increases with an increase in the NaCl concentration for both static and dynamic conditions, which indicates the compactness of the formed oxide film increases with the increase in the NaCl concentration, even though a close value of  $R_o$  is obtained for the

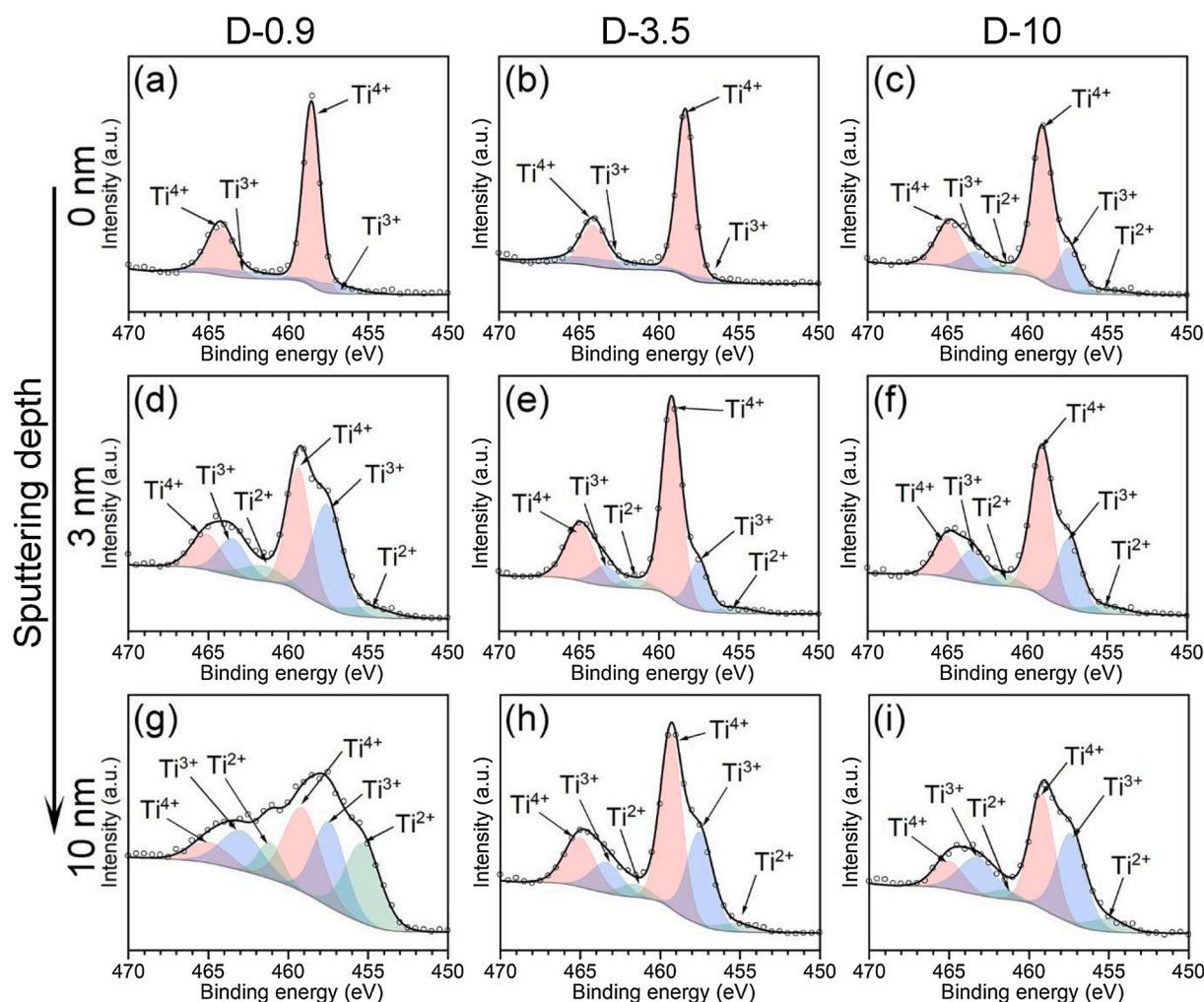


Fig. 14. XPS spectrum of Ti 2p region for SLMed Ti-6Al-4V after potentiodynamic polarization tests in dynamic condition with the NaCl concentrations of 0.9, 3.5, and 10 wt%, respectively.

samples tested in dynamic condition. Similar to the corrosion current density calculated in PD, the corrosion current density decreases with an increase in the NaCl concentration. Furthermore, the contents of  $\text{TiO}_2$  on the sample surface decrease with an increase in the NaCl concentration, even though a thick oxide film is formed in concentrated NaCl solution (e.g., 10 wt% NaCl), as shown in Fig. 15. However, an opposite result is observed in the following MS measurements. For example, the calculated thickness of the oxide film after PS decreases with an increase in the NaCl concentration. The possible reason causing the reversed results is that only  $\text{TiO}_2$  is in the oxide film, so that the dielectric constant ( $\epsilon$ ) of the  $\text{TiO}_2$  is equal to 60. But the contents of  $\text{TiO}_2$  in the practical oxide film decrease with an increase in the NaCl concentration, and the relative contents of the suboxides ( $\text{TiO}$  and  $\text{Ti}_2\text{O}_3$ ) increases. Therefore, a different result is present between the theoretical values and practical values.

The common corrosion characteristics of SLMed Ti-6Al-4V are the presented dark regions after PD, as shown in Figs. 8 and 9, where the dark regions are the initialization area accumulating the corrosion products. During the electrochemical tests, the corrosion products are generated and accumulated in the dark regions. According to the SEM, TEM and XPS analysis, the corrosion products are the oxides with different shapes. Also, the corrosion products and the dark areas increase with the increase in the NaCl concentration, as shown in Figs. 8 and 9. Such results indicate that the large contents of  $\text{Cl}^-$  in NaCl solution could promote the reactions between metal and electrolyte with

the increased thickness of the oxide film formed on the sample surface, even though  $\text{Cl}^-$  has a negative effect on the formed oxide film. According to the XPS analysis, the negative effect of  $\text{Cl}^-$  on corrosion is mainly presented as the dissolution of the  $\text{TiO}_2$ , which is distributed to the outer side of the formed oxide film (the contact phase with the electrolyte).

#### 4.3. Effect of electrolyte state on the formed oxide film

Since the dynamic electrolyte promotes and strengthens the diffusion of the ions and depolarizer (e.g., oxygen ions, cations) [77], the  $R_o$  value measured in the dynamic electrolyte condition is lower than that in the counterpart, and hence the corrosion process is accelerated. Similarly, the thickness of the oxide film formed in the dynamic condition is lower than that formed in the static condition, as shown in Figs. 10 and 11. This is also because the dynamic condition promotes the reaction between metal and electrolyte. However, according to the fitted results from EIS in Table 1, the  $R_o$  value tested in static conditions is doubled either from the NaCl concentration of 0.9 wt% increase to 3.5 wt%, or from 3.5 wt% increase to 10 wt%. However, the  $R_o$  value has a similar result under all different NaCl concentrations in the dynamic condition. The results indicate that the dynamic condition has a negative effect on corrosion, the resistance to corrosion decreases with an increase in the NaCl concentration although the  $R_o$  value is similar. Interestingly, the relative content of  $\text{TiO}_2$  in the oxide film under dynamic conditions is

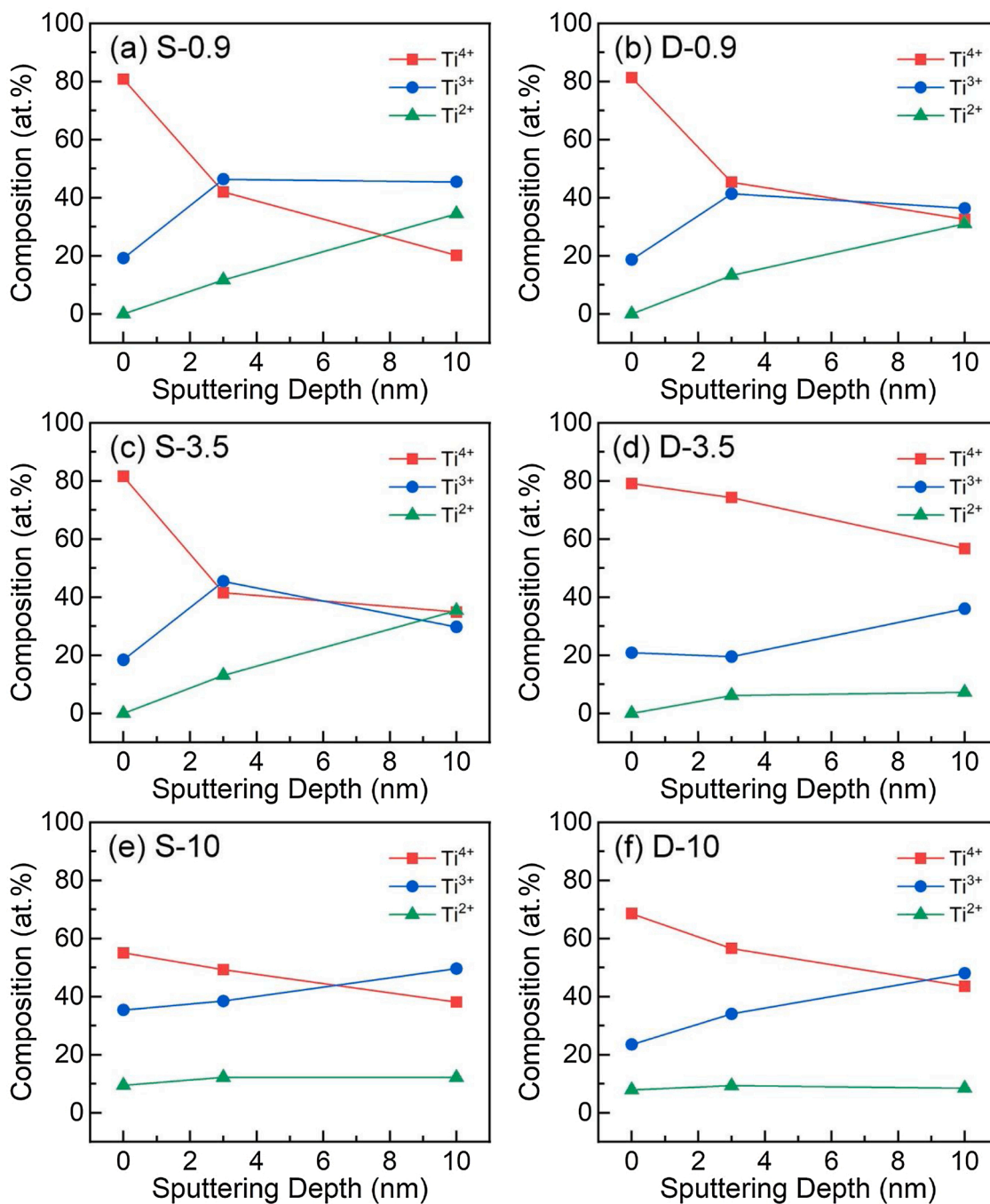


Fig. 15. Compositional distributions of Ti oxide from XPS results.

higher than that in static conditions for all NaCl solutions with different concentrations, as shown in Fig. 15. This finding indicates that the dynamic condition could increase the reaction kinetics and diffusion of oxygen. Therefore, a relatively higher content of TiO<sub>2</sub> is detected in all tested samples under dynamic conditions. Interestingly, the corrosion products under dynamic conditions (Fig. 9) are flatter than the ones formed under static conditions (Fig. 8). Such a finding could be attributed to a faster film growth in the concave region and oppositely for the convex site [78], and the dynamic condition significantly promotes the kinetics of the film growth.

Furthermore, the  $i_{corr}$  value measured from PD (Fig. 2) indicates that the corrosion resistance of the oxide film formed under the dynamic condition is inferior to the one formed under the static condition. A similar result is also found by comparing the  $N_D$  value obtained from MS

tests (Fig. 5), the oxide film formed under the dynamic condition has more defects than the one formed under the static condition. Furthermore, XPS results indicate that the oxide films formed under the dynamic conditions have a relatively higher fraction of TiO<sub>2</sub>, and the sample tested under the static and dynamic conditions have the same thickness of the oxide film when tested in 10 wt% NaCl solution. Compare with the results from the tests under the static condition, the above results from the tests under the dynamic condition suggest the oxide film growth is faster and has more defects under the dynamic condition. For example, similar  $R_o$  values and lower  $i_{corr}$  values for all NaCl concentrations, similar oxide thickness, etc.

## 5. Conclusions

The electrochemical behavior of the selective laser melting produced (SLMed) Ti-6Al-4V and the properties of the formed oxide film were investigated in the NaCl solutions with concentrations of 0.9, 3.5 and 10 wt% respectively and in different electrolyte conditions (static and dynamic). The main conclusions are summarized as follows:

- (1) The electrochemical results indicate that the corrosion behavior of SLMed Ti-6Al-4V is closely related to the NaCl concentration and to the flowing state of the electrolyte. Both the corrosion resistance and the formed oxide film thickness increase with the increase in the NaCl concentration. The difference in the oxide film thickness between the samples tested in static and dynamic conditions diminishes with the increase in the NaCl concentration.
- (2) Compared with the oxide film formed in the dynamic condition, a slightly higher thickness and better corrosion resistance of the formed oxide film is formed in the static condition. The oxide film formed under the static condition has also better quality (fewer defects with better corrosion resistance) than the one formed under the dynamic condition. The reason is that the dynamic condition promotes the reaction kinetics between the matrix and electrolyte, together with the aggressive properties of halide ions (e.g.,  $\text{Cl}^-$ ), which results in inferior corrosion resistance of the sample tested under the dynamic condition.
- (3) The relative contents of  $\text{TiO}_2$  in the oxide film under the dynamic conditions are higher than that under the static conditions for all NaCl solutions with different concentrations. This means that the oxide film formation is more compact under the static conditions than the one under the dynamic conditions for all NaCl solutions with different concentrations. Furthermore, the relative content of the  $\text{TiO}_2$  decreases as the NaCl concentration increases. Based on the electrochemical results, the oxide film formed under the dynamic condition is less resistant to corrosion compared with the one formed under the static condition.

## Data availability

The raw/processed data required to reproduce these findings cannot be shared at this time as the data also forms part of an ongoing study.

## CRedit authorship contribution statement

**P. Qin:** Conceptualization, Methodology, Investigation, Writing - original draft, Writing - review & editing. **L.Y. Chen:** Methodology, Writing - review & editing. **Y.J. Liu:** Writing - review & editing. **Z. Jia:** Writing - review & editing. **S.X. Liang:** Writing - review & editing. **C.H. Zhao:** Writing - review & editing. **H. Sun:** Writing - review & editing. **L. C. Zhang:** Conceptualization, Methodology, Investigation, Writing - original draft, Writing - review & editing, Supervision.

## Declaration of Competing Interest

The authors declare no competing financial interests or personal relationships that could have appeared to influence the work reported in this article.

## Acknowledgments

The authors would like to acknowledge the financial support provided by the Open Foundation of Guangxi Key Laboratory of Processing for Non-ferrous Metals and Featured Materials (Grant No. 2021GXY-SOF03) and Jiangsu Province six talent peaks project (XCL-117). P. Qin is grateful for the support of the ECU Postgraduate Research Scholarship. The authors acknowledge the facilities, and the scientific and

technical assistance of the Microscopy Australia at the Centre for Microscopy, Characterization & Analysis, The University of Western Australia, a facility funded by the University, State and Commonwealth Governments.

## References

- [1] J. Sun, X. Zhu, L. Qiu, F. Wang, Y. Yang, L. Guo, The microstructure transformation of selective laser melted Ti-6Al-4V alloy, *Mater. Today Commun.* 19 (2019) 277–285, <https://doi.org/10.1016/j.mtcomm.2019.02.006>.
- [2] X. Yan, C. Shi, T. Liu, Y. Ye, C. Chang, W. Ma, C. Deng, S. Yin, H. Liao, M. Liu, Effect of heat treatment on the corrosion resistance behavior of selective laser melted Ti6Al4V ELI, *Surf. Coat. Tech.* 396 (2020), 125955, <https://doi.org/10.1016/j.surfcoat.2020.125955>.
- [3] J. Ureña, S. Tsipas, A.M. Pinto, F. Toptan, E. Gordo, A. Jiménez Morales, Corrosion and tribocorrosion behaviour of  $\beta$ -type Ti-Nb and Ti-Mo surfaces designed by diffusion treatments for biomedical applications, *Corros. Sci.* 140 (2018) 51–60, <https://doi.org/10.1016/j.corsci.2018.06.024>.
- [4] H.M. Hamza, K.M. Deen, W. Haider, Microstructural examination and corrosion behavior of selective laser melted and conventionally manufactured Ti6Al4V for dental applications, *Mater. Sci. Eng. C* 113 (2020), 110980, <https://doi.org/10.1016/j.msec.2020.110980>.
- [5] L.C. Zhang, L.Y. Chen, L. Wang, Surface modification of titanium and titanium alloys: technologies, developments, and future interests, *Adv. Eng. Mater.* 22 (2020), 1901258, <https://doi.org/10.1002/adem.201901258>.
- [6] J. Li, X. Zhou, M. Brochu, N. Provatas, Y.F. Zhao, Solidification microstructure simulation of Ti-6Al-4V in metal additive manufacturing: a review, *Addit. Manuf.* 31 (2020), 100989, <https://doi.org/10.1016/j.addma.2019.100989>.
- [7] Y.J. Liu, Y.S. Zhang, L.C. Zhang, Transformation-induced plasticity and high strength in beta titanium alloy manufactured by selective laser melting, *Materialia* 6 (2019), 100299, <https://doi.org/10.1016/j.mtla.2019.100299>.
- [8] W.N. Zhang, L.Z. Wang, Z.X. Feng, Y.M. Chen, Research progress on selective laser melting (SLM) of magnesium alloys: a review, *Optik* 207 (2020), 163842, <https://doi.org/10.1016/j.ijleo.2019.163842>.
- [9] J.C. Wang, Y.J. Liu, P. Qin, S.X. Liang, T.B. Sercombe, L.C. Zhang, Selective laser melting of Ti-35Nb composite from elemental powder mixture: microstructure, mechanical behavior and corrosion behavior, *Mater. Sci. Eng. A* 760 (2019) 214–224, <https://doi.org/10.1016/j.msea.2019.06.001>.
- [10] N. Hafeez, J. Liu, L.Q. Wang, D. Wei, Y. Tang, W. Lu, L.C. Zhang, Superelastic response of low-modulus porous beta-type Ti-35Nb-2Ta-3Zr alloy fabricated by laser powder bed fusion, *Addit. Manuf.* 34 (2020), 101264, <https://doi.org/10.1016/j.addma.2020.101264>.
- [11] L.Y. Chen, Y.W. Cui, L.C. Zhang, Recent development in beta titanium alloys for biomedical applications, *Metals* 10 (2020) 1139, <https://doi.org/10.3390/met10091139>.
- [12] D. Gu, H. Zhang, D. Dai, C. Ma, H. Zhang, Y. Li, S. Li, Anisotropic corrosion behavior of Sc and Zr modified Al-Mg alloy produced by selective laser melting, *Corros. Sci.* 170 (2020), 108657, <https://doi.org/10.1016/j.corsci.2020.108657>.
- [13] O. Gharbi, D. Jiang, D.R. Feenstra, S.K. Kairy, Y. Wu, C.R. Hutchinson, N. Birbilis, On the corrosion of additively manufactured aluminium alloy AA2024 prepared by selective laser melting, *Corros. Sci.* 143 (2018) 93–106, <https://doi.org/10.1016/j.corsci.2018.08.019>.
- [14] P. Fathi, M. Rafieezad, X. Duan, M. Mohammadi, A.M. Nasiri, On microstructure and corrosion behaviour of AlSi10Mg alloy with low surface roughness fabricated by direct metal laser sintering, *Corros. Sci.* 157 (2019) 126–145, <https://doi.org/10.1016/j.corsci.2019.05.032>.
- [15] P. Qin, L.Y. Chen, C.H. Zhao, Y.J. Liu, C.D. Cao, H. Sun, L.C. Zhang, Corrosion behavior and mechanism of selective laser melted Ti35Nb alloy produced using pre-alloyed and mixed powder in Hank's solution, *Corros. Sci.* 189 (2021), 109609, <https://doi.org/10.1016/j.corsci.2021.109609>.
- [16] V. Cruz, Q. Chao, N. Birbilis, D. Fabijanic, P.D. Hodgson, S. Thomas, Electrochemical studies on the effect of residual stress on the corrosion of 316L manufactured by selective laser melting, *Corros. Sci.* 164 (2020), 108314, <https://doi.org/10.1016/j.corsci.2019.108314>.
- [17] R.I. Revilla, B. Wouters, F. Andreatta, A. Lanzutti, L. Fedrizzi, I. De Graeve, EIS comparative study and critical Equivalent Electrical Circuit (EEC) analysis of the native oxide layer of additive manufactured and wrought 316L stainless steel, *Corros. Sci.* 167 (2020), 108480, <https://doi.org/10.1016/j.corsci.2020.108480>.
- [18] Z. Duan, C. Man, C. Dong, Z. Cui, D. Kong, L. Wang, X. Wang, Pitting behavior of SLM 316L stainless steel exposed to chloride environments with different aggressiveness: pitting mechanism induced by gas pores, *Corros. Sci.* 167 (2020), 108520, <https://doi.org/10.1016/j.corsci.2020.108520>.
- [19] X. Dong, Q. Sun, Y. Zhou, Y. Qu, H. Shi, B. Zhang, S. Xu, W. Liu, N. Li, J. Yan, Influence of microstructure on corrosion behavior of biomedical Co-Cr-Mo-W alloy fabricated by selective laser melting, *Corros. Sci.* 170 (2020), 108688, <https://doi.org/10.1016/j.corsci.2020.108688>.
- [20] T. Fujieda, M. Chen, H. Shiratori, K. Kuwabara, K. Yamanaka, Y. Koizumi, A. Chiba, S. Watanabe, Mechanical and corrosion properties of CoCrFeNiTi-based high-entropy alloy additive manufactured using selective laser melting, *Addit. Manuf.* 25 (2019) 412–420, <https://doi.org/10.1016/j.addma.2018.10.023>.
- [21] Y. Lu, S. Wu, Y. Gan, S. Zhang, S. Guo, J. Lin, J. Lin, Microstructure, mechanical property and metal release of As-SLM CoCrW alloy under different solution treatment conditions, *J. Mech. Behav. Biomed.* 55 (2016) 179–190, <https://doi.org/10.1016/j.jmbbm.2015.10.019>.

- [22] X. Gao, X. Lin, J. Yu, Y. Li, Y. Hu, W. Fan, S. Shi, W. Huang, Selective Laser Melting (SLM) of in-situ beta phase reinforced Ti/Zr-based bulk metallic glass matrix composite, *Scr. Mater.* 171 (2019) 21–25, <https://doi.org/10.1016/j.scriptamat.2019.06.007>.
- [23] J.J. Marattukalam, V. Pacheco, D. Karlsson, L. Riekehr, J. Lindwall, F. Forsberg, U. Jansson, M. Sahlberg, B. Hjørvarsson, Development of process parameters for selective laser melting of a Zr-based bulk metallic glass, *Addit. Manuf.* 33 (2020), 101124, <https://doi.org/10.1016/j.addma.2020.101124>.
- [24] S.X. Liang, X. Wang, W. Zhang, Y.J. Liu, W. Wang, L.C. Zhang, Selective laser melting manufactured porous Fe-based metallic glass matrix composite with remarkable catalytic activity and reusability, *Appl. Mater. Today* 19 (2020), 100543, <https://doi.org/10.1016/j.apmt.2019.100543>.
- [25] A. Ataei, Y. Li, C. Wen, A comparative study on the nanoindentation behavior, wear resistance and in vitro biocompatibility of SLM manufactured CP-Ti and EBM manufactured Ti64 gyroid scaffolds, *Acta Biomater.* 97 (2019) 587–596, <https://doi.org/10.1016/j.actbio.2019.08.008>.
- [26] A.M. Khorasani, I. Gibson, U.S. Awan, A. Ghaderi, The effect of SLM process parameters on density, hardness, tensile strength and surface quality of Ti-6Al-4V, *Addit. Manuf.* 25 (2019) 176–186, <https://doi.org/10.1016/j.addma.2018.09.002>.
- [27] D.I. Seo, J.B. Lee, Corrosion characteristics of additive-manufactured Ti-6Al-4V using microdroplet cell and critical pitting-temperature techniques, *J. Electrochem. Soc.* 166 (2019) C428–C433, <https://doi.org/10.1149/2.0571913jes>.
- [28] Y. Yang, Y. Chen, J.X. Zhang, X.H. Gu, P. Qin, N.W. Dai, X.P. Li, J.P. Kruth, L. C. Zhang, Improved corrosion behavior of ultrafine-grained eutectic Al-12Si alloy produced by selective laser melting, *Mater. Des.* 146 (2018) 239–248, <https://doi.org/10.1016/j.matdes.2018.03.025>.
- [29] T. Rubben, R.I. Revilla, I. De Graeve, Influence of heat treatments on the corrosion mechanism of additive manufactured AlSi10Mg, *Corros. Sci.* 147 (2019) 406–415, <https://doi.org/10.1016/j.corsci.2018.11.038>.
- [30] M. Laleh, A.E. Hughes, W. Xu, P. Cizek, M.Y. Tan, Unanticipated drastic decline in pitting corrosion resistance of additively manufactured 316L stainless steel after high-temperature post-processing, *Corros. Sci.* 165 (2020), 108412, <https://doi.org/10.1016/j.corsci.2019.108412>.
- [31] L.C. Zhang, L.Y. Chen, A review on biomedical titanium alloys: recent progress and prospect, *Adv. Eng. Mater.* 21 (2019), 1801215, <https://doi.org/10.1002/adem.201801215>.
- [32] N.W. Dai, L.C. Zhang, J.X. Zhang, Q.M. Chen, M.L. Wu, Corrosion behavior of selective laser melted Ti-6Al-4V alloy in NaCl solution, *Corros. Sci.* 102 (2016) 484–489, <https://doi.org/10.1016/j.corsci.2015.10.041>.
- [33] H. Zhang, C. Man, C. Dong, L. Wang, W. Li, D. Kong, L. Wang, X. Wang, The corrosion behavior of Ti6Al4V fabricated by selective laser melting in the artificial saliva with different fluoride concentrations and pH values, *Corros. Sci.* 179 (2021), 109097, <https://doi.org/10.1016/j.corsci.2020.109097>.
- [34] W. Wan, J. Xiong, Z. Guo, L. Tang, H. Du, Research on the contributions of corrosion, erosion and synergy to the erosion-corrosion degradation of Ti(C,N)-based cermets, *Wear* 326–327 (2015) 36–43, <https://doi.org/10.1016/j.wear.2014.12.041>.
- [35] W. Wan, J. Xiong, Y. Li, Q. Tang, M. Liang, Erosion-corrosion behavior of Ti(C,N)-based cermets containing different secondary carbides, *Int. J. Refract. Metals Hard* 66 (2017) 180–187, <https://doi.org/10.1016/j.ijrmhm.2017.03.018>.
- [36] W. Apeador, E. Delgado, C. Amaya, Effect of cavitation on the corrosion behavior of Ti (CN)/TiNb (CN) multilayer in seawater, *Int. J. Electrochem. Sci.* 9 (2014) 4558–4565.
- [37] L.Y. Chen, H.Y. Zhang, C. Zheng, H.Y. Yang, P. Qin, C. Zhao, S. Lu, S.X. Liang, L. Chai, L.C. Zhang, Corrosion behavior and characteristics of passive films of laser powder bed fusion produced Ti-6Al-4V in dynamic Hank's solution, *Mater. Des.* 208 (2021), 109907, <https://doi.org/10.1016/j.matdes.2021.109907>.
- [38] F. Toptan, A.C. Alves, Ó. Carvalho, F. Bartolomeu, A.M.P. Pinto, F. Silva, G. Miranda, Corrosion and tribocorrosion behaviour of Ti6Al4V produced by selective laser melting and hot pressing in comparison with the commercial alloy, *J. Mater. Process. Tech.* 266 (2019) 239–245, <https://doi.org/10.1016/j.jmatprotec.2018.11.008>.
- [39] J. Yang, H. Yang, H. Yu, Z. Wang, X. Zeng, Corrosion behavior of additive manufactured Ti-6Al-4V alloy in NaCl solution, *Metall. Mater. Trans. A* 48 (2017) 3583–3593, <https://doi.org/10.1007/s11661-017-4087-9>.
- [40] J. Li, X. Lin, P. Guo, M. Song, W. Huang, Electrochemical behaviour of laser solid formed Ti-6Al-4V alloy in a highly concentrated NaCl solution, *Corros. Sci.* 142 (2018) 161–174, <https://doi.org/10.1016/j.corsci.2018.07.023>.
- [41] Y. Chen, J.X. Zhang, N.W. Dai, P. Qin, H. Attar, L.C. Zhang, Corrosion behaviour of selective laser melted Ti-TiB biocomposite in simulated body fluid, *Electrochim. Acta* 232 (2017) 89–97, <https://doi.org/10.1016/j.electacta.2017.02.112>.
- [42] P. Renner, S. Jha, Y. Chen, A. Raut, S. Mehta, H. Liang, A review on corrosion and wear of additively manufactured alloys, *J. Tribol.* (2021) 1–54, <https://doi.org/10.1115/1.4050503>.
- [43] A. Gebert, S. Oswald, A. Helth, A. Voss, P.F. Gostin, M. Rohnke, J. Janek, M. Calin, J. Eckert, Effect of indium (In) on corrosion and passivity of a beta-type Ti-Nb alloy in Ringer's solution, *Appl. Surf. Sci.* 335 (2015) 213–222, <https://doi.org/10.1016/j.apsusc.2015.02.058>.
- [44] T. Hanawa, K. Asami, K. Asaoka, Repassivation of titanium and surface oxide film regenerated in simulated biofluid, *J. Biomed. Mater. Res.* 40 (1998) 530–538, [https://doi.org/10.1002/\(SICI\)1097-4636\(19980615\)40:4<530::AID-JBM3>3.0.CO;2-G](https://doi.org/10.1002/(SICI)1097-4636(19980615)40:4<530::AID-JBM3>3.0.CO;2-G).
- [45] M. Metikos Huković, A. Kwokal, J. Piljac, The influence of niobium and vanadium on passivity of titanium-based implants in physiological solution, *Biomaterials* 24 (2003) 3765–3775, [https://doi.org/10.1016/S0142-9612\(03\)00252-7](https://doi.org/10.1016/S0142-9612(03)00252-7).
- [46] W. Ding, Z. Wang, G. Chen, W. Cai, C. Zhang, Q. Tao, X. Qu, M. Qin, Oxidation behavior of low-cost CP-Ti powders for additive manufacturing via fluidization, *Corros. Sci.* 178 (2021), 109080, <https://doi.org/10.1016/j.corsci.2020.109080>.
- [47] N.W. Dai, L.C. Zhang, J.X. Zhang, X. Zhang, Q.Z. Ni, Y. Chen, M.L. Wu, C. Yang, Distinction in corrosion resistance of selective laser melted Ti-6Al-4V alloy on different planes, *Corros. Sci.* 111 (2016) 703–710, <https://doi.org/10.1016/j.corsci.2016.06.009>.
- [48] P. Qin, Y.J. Liu, T.B. Sercombe, Y.H. Li, C.W. Zhang, C.D. Cao, H.Q. Sun, L. C. Zhang, Improved corrosion resistance on selective laser melting produced Ti-5Cu alloy after heat treatment, *ACS Biomater. Sci. Eng.* 4 (2018) 2633–2642, <https://doi.org/10.1021/acsbomaterials.8b00319>.
- [49] Q.T. Song, J. Xu, (TiZrNbTa)90Mo10 high-entropy alloy: Electrochemical behavior and passive film characterization under exposure to Ringer's solution, *Corros. Sci.* 167 (2020), 108513, <https://doi.org/10.1016/j.corsci.2020.108513>.
- [50] L. Guan, Y. Li, G. Wang, Y. Zhang, L.C. Zhang, pH dependent passivation behavior of niobium in acid fluoride-containing solutions, *Electrochim. Acta* 285 (2018) 172–184, <https://doi.org/10.1016/j.electacta.2018.07.221>.
- [51] L. Wang, H. Yu, S. Wang, B. Chen, Y. Wang, W. Fan, D. Sun, Quantitative analysis of local fine structure on diffusion of point defects in passive film on Ti, *Electrochim. Acta* 314 (2019) 161–172, <https://doi.org/10.1016/j.electacta.2019.05.048>.
- [52] D.D. Macdonald, The history of the Point Defect Model for the passive state: a brief review of film growth aspects, *Electrochim. Acta* 56 (2011) 1761–1772, <https://doi.org/10.1016/j.electacta.2010.11.005>.
- [53] M. Wang, Z. Wang, X. Gong, Z. Guo, The intensification technologies to water electrolysis for hydrogen production – a review, *Renew. Sust. Energ. Rev.* 29 (2014) 573–588, <https://doi.org/10.1016/j.rser.2013.08.090>.
- [54] P. Qin, Y. Chen, Y.J. Liu, J.X. Zhang, L.Y. Chen, Y. Li, X.H. Zhang, C.D. Cao, H. Q. Sun, L.C. Zhang, Resemblance in corrosion behavior of selective laser melted and traditional monolithic  $\beta$  Ti-24Nb-4Zr-8Sn alloy, *ACS Biomater. Sci. Eng.* 5 (2019) 1141–1149, <https://doi.org/10.1021/acsbomaterials.8b01341>.
- [55] B.N. Popov, *Corrosion Engineering: Principles And Solved Problems*, Elsevier, 2015.
- [56] I.C. Chung, C.K. Chung, Y.K. Su, Effect of current density and concentration on microstructure and corrosion behavior of 6061 Al alloy in sulfuric acid, *Surf. Coat. Tech.* 313 (2017) 299–306, <https://doi.org/10.1016/j.surfcoat.2017.01.114>.
- [57] B. Munirathnam, R. Narayanan, L. Neelakantan, Electrochemical and semiconducting properties of thin passive film formed on titanium in chloride medium at various pH conditions, *Thin Solid Films* 598 (2016) 260–270, <https://doi.org/10.1016/j.tsf.2015.12.025>.
- [58] D.D. Macdonald, The point defect model for the passive state, *J. Electrochem. Soc.* 139 (1992) 3434–3449, <https://doi.org/10.1149/1.2069096>.
- [59] J.R. Galvele, R.M. Torresi, R.M. Carranza, Passivity breakdown, its relation to pitting and stress-corrosion-cracking processes, *Corros. Sci.* 31 (1990) 563–571, [https://doi.org/10.1016/0010-938X\(90\)90163-Y](https://doi.org/10.1016/0010-938X(90)90163-Y).
- [60] X. Gai, Y. Bai, J. Li, S. Li, W. Hou, Y. Hao, X. Zhang, R. Yang, R.D.K. Misra, Electrochemical behaviour of passive film formed on the surface of Ti-6Al-4V alloys fabricated by electron beam melting, *Corros. Sci.* 145 (2018) 80–89, <https://doi.org/10.1016/j.corsci.2018.09.010>.
- [61] X. Gong, Y. Li, Y. Nie, Z. Huang, F. Liu, L. Huang, L. Jiang, H. Mei, Corrosion behaviour of CoCrMo alloy fabricated by electron beam melting, *Corros. Sci.* 139 (2018) 68–75, <https://doi.org/10.1016/j.corsci.2018.04.033>.
- [62] B. Hirschorn, M.E. Orazem, B. Tribollet, V. Vivier, I. Frateur, M. Musiani, Determination of effective capacitance and film thickness from constant-phase-element parameters, *Electrochim. Acta* 55 (2010) 6218–6227, <https://doi.org/10.1016/j.electacta.2009.10.065>.
- [63] Y. Chen, J.X. Zhang, X.H. Gu, N.W. Dai, P. Qin, L.C. Zhang, Distinction of corrosion resistance of selective laser melted Al-12Si alloy on different planes, *J. Alloys. Compd.* 747 (2018) 648–658, <https://doi.org/10.1016/j.jallcom.2018.03.062>.
- [64] A. Fattah-alhosseini, M.A. Golozar, A. Saatchi, K. Raieisi, Effect of solution concentration on semiconducting properties of passive films formed on austenitic stainless steels, *Corros. Sci.* 52 (2010) 205–209, <https://doi.org/10.1016/j.corsci.2009.09.003>.
- [65] L. Thijs, F. Verhaeghe, T. Craeghs, J. Van Humbeeck, J.P. Kruth, A study of the microstructural evolution during selective laser melting of Ti-6Al-4V, *Acta Mater.* 58 (2010) 3303–3312, <https://doi.org/10.1016/j.actamat.2010.02.004>.
- [66] S. Liu, Y.C. Shin, Additive manufacturing of Ti6Al4V alloy: a review, *Mater. Des.* 164 (2019), 107552, <https://doi.org/10.1016/j.matdes.2018.107552>.
- [67] M. Laleh, A.E. Hughes, S. Yang, J. Li, W. Xu, I. Gibson, M.Y. Tan, Two and three-dimensional characterisation of localised corrosion affected by lack-of-fusion pores in 316L stainless steel produced by selective laser melting, *Corros. Sci.* 165 (2020), 108394, <https://doi.org/10.1016/j.corsci.2019.108394>.
- [68] Y.J. Liu, S.J. Li, H.L. Wang, W.T. Hou, Y.L. Hao, R. Yang, T.B. Sercombe, L. C. Zhang, Microstructure, defects and mechanical behavior of beta-type titanium porous structures manufactured by electron beam melting and selective laser melting, *Acta Mater.* 113 (2016) 56–67, <https://doi.org/10.1016/j.actamat.2016.04.029>.
- [69] B. Zhou, J. Zhou, H. Li, F. Lin, A study of the microstructures and mechanical properties of Ti6Al4V fabricated by SLM under vacuum, *Mater. Sci. Eng. A* 724 (2018) 1–10, <https://doi.org/10.1016/j.msea.2018.03.021>.
- [70] Z.Y. Zhao, L. Li, P.K. Bai, Y. Jin, L.Y. Wu, J. Li, R.G. Guan, H.Q. Qu, The heat treatment influence on the microstructure and hardness of TC4 titanium alloy manufactured via selective laser melting, *Materials* 11 (2018) 1318, <https://doi.org/10.3390/ma11081318>.

- [71] Z.B. Wang, H.X. Hu, Y.G. Zheng, W. Ke, Y.X. Qiao, Comparison of the corrosion behavior of pure titanium and its alloys in fluoride-containing sulfuric acid, *Corros. Sci.* 103 (2016) 50–65, <https://doi.org/10.1016/j.corsci.2015.11.003>.
- [72] J. William, D. Callister, D.G. Rethwisch, *Materials Science and Engineering: An Introduction*, 8 ed., Donald Fowley, 2009.
- [73] Y. Lu, J. Dong, W. Ke, Effects of Cl<sup>-</sup> ions on the corrosion behaviour of low alloy steel in deaerated bicarbonate solutions, *J. Mater. Sci. Technol.* 32 (2016) 341–348, <https://doi.org/10.1016/j.jmst.2015.11.015>.
- [74] Y. Ma, Y. Li, F. Wang, Corrosion of low carbon steel in atmospheric environments of different chloride content, *Corros. Sci.* 51 (2009) 997–1006, <https://doi.org/10.1016/j.corsci.2009.02.009>.
- [75] P. Marcus, V. Maurice, H.H. Strehblow, Localized corrosion (pitting): a model of passivity breakdown including the role of the oxide layer nanostructure, *Corros. Sci.* 50 (2008) 2698–2704, <https://doi.org/10.1016/j.corsci.2008.06.047>.
- [76] S. Zhang, L. Hou, H. Du, H. Wei, B. Liu, Y. Wei, A study on the interaction between chloride ions and CO<sub>2</sub> towards carbon steel corrosion, *Corros. Sci.* 167 (2020), 108531, <https://doi.org/10.1016/j.corsci.2020.108531>.
- [77] J. Li, I. Mutreja, S. Tredinnick, M. Jermy, G.J. Hooper, T.B.F. Woodfield, Hydrodynamic control of titania nanotube formation on Ti-6Al-4V alloys enhances osteogenic differentiation of human mesenchymal stromal cells, *Mater. Sci. Eng. C* 109 (2020), 110562, <https://doi.org/10.1016/j.msec.2019.110562>.
- [78] B. Zhang, J. Wang, B. Wu, X. Guo, Y. Wang, D. Chen, Y. Zhang, K. Du, E. Oguzie, X. Ma, Unmasking chloride attack on the passive film of metals, *Nat. Commun.* 9 (2018) 2559, <https://doi.org/10.1038/s41467-018-04942-x>.